

Perspective

Interactions of Single Particle with Organic Matters: A Facile Bottom-Up Approach to Low Dimensional Nanostructures

Shugo Sakaguchi, Koshi Kamiya, Tsuneaki Sakurai  and Shu Seki * 

Department of Molecular Engineering, Graduate School of Engineering, Kyoto University, Nishikyo-ku, Kyoto 615-8510, Japan; sakaguchi.shugo.84a@st.kyoto-u.ac.jp (S.S.); kamiya.koshi.35c@st.kyoto-u.ac.jp (K.K.); sakurai-t@moleng.kyoto-u.ac.jp (T.S.)

* Correspondence: seki@moleng.kyoto-u.ac.jp; Tel.: +81-75-383-2572

Received: 2 December 2019; Accepted: 20 January 2020; Published: 5 February 2020



Abstract: A particle induces a pack of chemical reactions in nanospace: chemical reactions confined into extremely small space provide an ultimate technique for the nanofabrication of organic matter with a variety of functions. Since the discovery of particle accelerators, an extremely high energy density can be deposited, even by a single isolated particle with MeV-ordered kinetic energy. However, this was considered to cause severe damages to organic molecules due to its relatively small bond energies, and lack of ability to control the reactions precisely to form the structures while retaining physico-chemical molecular functionalities. Practically, the severely damaged area along a particle trajectory: a core of a particle track has been simply visualized for the detection/dosimetry of an incident particle to the matters, or been removed to lead nanopores and functionalized by refilling/grafting of fresh organic/inorganic materials. The use of intra-track reactions in the so-called “penumbra” or “halo” area of functional organic materials has been realized and provided us with novel and facile protocols to provide low dimensional nano-materials with perfect size controllability in the 21st century. These protocols are now referred to as single particle nanofabrication technique (SPNT) and/or single particle triggered linear polymerization technique (STLiP), paving the way towards a new approach for nanomaterials with desired functionalities from original molecules. Herein, we report on the extremely wide applicability of SPNT/STLiP protocols for the future development of materials for opto-electronic, catalytic, and biological applications among others.

Keywords: nanomaterial; nanowire; charged particle; stopping power; crosslinking; polymerization; aspect ratio; stimuli sensitive; sensor; macromolecules

1. Spatial Energy Distribution Released by High Energy Particle in Organic Substances

Since the dawn of quantum mechanical aspects of atoms and molecules, interactions of ionizing radiations with condensed matters has been at the center of analytical techniques, in order to determine the electronic structures of them [1–4]. Particularly the Coulombic interactions between charged particles with a relatively high momentum and electrons confined in their orbitals have been discussed precisely in terms of the experimental energy loss of the incident charged particles, and/or cross section of ionization events induced in the target condensed matters [5,6]. For the quantitative experimental analysis of the loss/events in the system, X-rays/ γ -rays and high energy electron beams have often been popular choices because of the homogeneity of the released energy from the ionizing radiation into the target matters, which helps statistical counting of the events/resulting products and intermediates by conventional analysis protocols such as spectroscopic/microscopic techniques [7,8]. In contrast to the classical ionizing radiation applied to reveal atomic/molecular structures, heavy charged particles

also play a significant role to clarify the structures, as evident in the initial success of Rutherford scattering experiments via momentum transfer from an incident charged particle to the target atoms. Thus, the energy dissipation processes from the incident charged particles draw the attention of scientists working on condensed matter physics, nuclear physics, astrophysics, etc. For instance, the visualization of high energy charged particle tracks in organic/inorganic matters was successfully applied to assess the energy/momentum of the incident charged particles, giving clear evidence of nuclear reactions caused by the particles [9]. By 20th century, the theoretical background used for interpreting these interactions has been well developed in correlation with experimental observation, leading to sophisticated formulations. The initial benchmark of the formulation was first established by Bethe [10,11], starting from a simple binary elastic collision model in terms of transferred energy (T) from one particle to the other. When we consider elastic collisions between an incident particle and an electron in the target atoms, its differential cross section ($\Delta\sigma$) of the incident particle can be represented as,

$$d\sigma = \frac{2\pi Z_1^2 e^4}{m_e v^2} \frac{dT}{T^2}, \quad (1)$$

where Z_1 and v are the atomic number and the velocity of the incident particle, while m_e and e are mass of electron and an elementary charge, respectively.

Now, the ionization events in the condensed phases as well as successive chemical reaction in the matter are considered as inelastic collision events for an incident particle [12]. Ionization cross section in classical Thomson model could be delivered by Equation (1) based on the Rutherford scattering scheme [2,13]. However, more detailed discussions were initiated by Born with quantum mechanical views of target substances with a general wave function of their frontier orbital: $\psi(\mathbf{r})$ which can be derived by a general Schrödinger equation as,

$$(\nabla^2 + k^2)\psi(\mathbf{r}) = U(\mathbf{r})\psi(\mathbf{r}), \quad V(\mathbf{r}) = \frac{\hbar^2 U(\mathbf{r})}{2\mu}, \quad (2)$$

and the solutions of Equation (2) are given with the use of Green's function of $G_{\pm}(\mathbf{r})$ and an incident plane-wave function $\phi_{inc}(\mathbf{r})$ as [14],

$$\psi(\mathbf{r}) = \phi_{inc}(\mathbf{r}) + \int G_{\pm}(\mathbf{r} - \mathbf{r}') U(\mathbf{r}') \psi(\mathbf{r}') d^3 r'. \quad (3)$$

Here we obtain,

$$G_{\pm}(\mathbf{r} - \mathbf{r}') = -\frac{1}{4\pi} \frac{\exp(\pm ik|\mathbf{r} - \mathbf{r}'|)}{|\mathbf{r} - \mathbf{r}'|}, \quad (4)$$

under the following requirements for $\phi(\mathbf{r})$ and $G_{\pm}(\mathbf{r})$ of

$$(\nabla^2 + k^2)\phi(\mathbf{r}) = 0, \quad (5)$$

and

$$(\nabla^2 + k^2)G_{\pm}(\mathbf{r} - \mathbf{r}') = \delta^d(\mathbf{r} - \mathbf{r}'). \quad (6)$$

Considering only the contribution of the outgoing wave function from \mathbf{r}' leading to $G_+(\mathbf{r})$, the solution of the above Schrödinger equation is given by Lippmann-Schwinger equation as [15],

$$\psi(\mathbf{r}) = \phi_{inc}(\mathbf{r}) + \int G_+(\mathbf{r} - \mathbf{r}') U(\mathbf{r}') \psi(\mathbf{r}') d^3 r'. \quad (7)$$

Here, we presume $\mathbf{r} \gg \mathbf{r}'$, the norm of displacement vector can be represented by,

$$|\mathbf{r} - \mathbf{r}'| = r - \mathbf{n} \cdot \mathbf{r}', \quad (8)$$

then we obtain a simplified expression of form for Green's function as,

$$G_+(\mathbf{r} - \mathbf{r}') = -\frac{1}{4\pi} \frac{\exp(ikr)}{r} \exp(-i\mathbf{k}\mathbf{n} \cdot \mathbf{r}'). \quad (9)$$

By substituting this into Equation (7), the resulting wave function of the target is represented as,

$$\psi(\mathbf{r}) = \phi_{inc}(\mathbf{r}) + \left[-\frac{1}{4\pi} \int \exp(-i\mathbf{k}\mathbf{n} \cdot \mathbf{r}') U(\mathbf{r}') \psi(\mathbf{r}') d^3r' \right] \frac{\exp(ikr)}{r}. \quad (10)$$

To lead an explicit analytical solution for $\psi(\mathbf{r})$ of electrons responsible to the first ionization energy of the target materials, we use the Born approximation to Equation (7), expanded with Born series [16], and take the first order expansion as an approximate as follows,

$$\psi(\mathbf{r}) = \phi_{inc}(\mathbf{r}) + \int G_+(\mathbf{r} - \mathbf{r}') U(\mathbf{r}') \phi_{inc}(\mathbf{r}') d^3r'. \quad (11)$$

By comparing Equation (11) to (10), provisionally, the solution has been obtained as,

$$\psi(\mathbf{r}) = \phi_{inc}(\mathbf{r}) + \left[-\frac{1}{4\pi} \int \exp(-i\mathbf{k}\mathbf{n} \cdot \mathbf{r}') U(\mathbf{r}') e^{i\mathbf{k}\cdot\mathbf{r}'} d^3r' \right] \frac{\exp(ikr)}{r}. \quad (12)$$

Here, \mathbf{n} is a unit vector. The wave vectors in the integrant can be substituted by,

$$\mathbf{K} = \mathbf{k}\mathbf{n} - \mathbf{k} = \mathbf{k}' - \mathbf{k}, \quad (13)$$

and the simplified wave function is given by,

$$\psi(\mathbf{r}) = \phi_{inc}(\mathbf{r}) + \left[-\frac{1}{4\pi} \int \exp(-i\mathbf{K} \cdot \mathbf{r}') U(\mathbf{r}') d^3r' \right] \frac{\exp(ikr)}{r}. \quad (14)$$

The second term in Equation (14) is responsible for the inelastic energy loss of an incident particle which can be transferred to the target. If we discuss the term separatory as a function of $f(\theta, \varphi)$, Equation (14) can be rewritten as,

$$\psi(\mathbf{r}) \simeq \exp(i\mathbf{k} \cdot \mathbf{r}) + f(\theta, \varphi) \frac{\exp(ikr)}{r} \quad (15)$$

and

$$f(\theta, \varphi) = -\frac{1}{4\pi} \int \exp(-i\mathbf{K} \cdot \mathbf{r}') U(\mathbf{r}') d^3r', \quad (16)$$

respectively. Now the differential inelastic cross section of $d\sigma$ can be formulated clearly as,

$$d\sigma = \frac{1}{16\pi^2} \left| \langle \phi_{\mathbf{k}'} | U | \phi_{\mathbf{k}} \rangle \right|^2 d\Omega, \quad (17)$$

where $d\Omega$ is the differential solid angle. With the measure of momentum of the incident particle prior after the collision events as p and p' , respectively, Equation (17) can be derived as,

$$d\sigma = \frac{\mu^2}{4\pi^2 \hbar^4} \frac{p'}{p} \left| \langle \phi_{\mathbf{k}'} | V | \phi_{\mathbf{k}} \rangle \right|^2, \quad (18)$$

where $V(\mathbf{r})$ is the Coulombic potential between the particles as represented simply by,

$$V = \frac{Z_1 Z_2 e^2}{r} - Z_1 \sum_{i=1}^{Z_2} \frac{e^2}{|\mathbf{r} - \mathbf{r}_i|}, \quad (19)$$

Then, the integration over \mathbf{r} can be written by,

$$\int \exp(i\mathbf{K} \cdot \mathbf{r}) \frac{d\mathbf{r}}{|\mathbf{r} - \mathbf{r}_i|} = \frac{4\pi}{K^2} \exp(i\mathbf{K} \cdot \mathbf{r}_i). \quad (20)$$

Thus, Equation (18) transforms into follows with an atomic matrix element called as the Fano factor: $|F_n(\mathbf{K})|^2$ [17,18].

$$d\sigma = \frac{4Z_1^2 \mu^2 e^4}{\hbar^4 K^4} \frac{p'}{p} |F_n(\mathbf{K})|^2 d\Omega \quad (21)$$

and

$$|F_n(\mathbf{K})|^2 = \int \sum_i \exp(i\mathbf{K} \cdot \mathbf{r}_i) u_n^* u_0 d\mathbf{r}_i, \quad (22)$$

where u is the eigenfunction of electron orbital in the target. Considering the energy and momentum consevation law, we obtain a relationship between K and Ω given as,

$$d(K^2) = \frac{pp'}{\pi} d\Omega. \quad (23)$$

Therefore Equation (21) is equivalent to:

$$d\sigma = \frac{4\pi Z_1^2 \mu^2 e^4}{\hbar^4 K^4} \frac{1}{p^2} |F_n(\mathbf{K})|^2 d(K^2). \quad (24)$$

The given kinetic energy transferred to an electron as $Q = \frac{\hbar^2 K^2}{2m_e}$ into Equation (24), $d\sigma$ can be finally appeared as,

$$d\sigma = \frac{2\pi Z_1^2 e^4}{m_e v^2} \frac{1}{Q^2} |F_n(Q)|^2 dQ. \quad (25)$$

Now, we have obtained the theoretical differential cross section of the incident particle in an inelastic collision event [18].

The statistical treatment of the collision events within the matter will lead to an overall energy loss of an incident particle along the particle trajectory. Now, the averaged energy loss (S) of the particle per unit length of the trajectory is defined by:

$$-\frac{dE}{dx} = N \int T d\sigma \equiv S, \quad (26)$$

where N is the number density of atoms in the target. In this study, the energy delivered by the incident particle to the molecular materials is predominantly consumed as ionization events, where the velocity of an incident particle is relatively larger than the angular momentum of electrons bound to the molecules. Here, we only treat the case of the larger velocity than the Massey's criterion [19], S is given from Equation (1) by,

$$S = \frac{2\pi Z_1^2 e^4}{m_e v^2} N \int_{T_{\min}}^{T_{\max}} \frac{dT}{T}, \quad (27)$$

where T_{\max} equals to $2m_e v^2$, and T_{\min} depends on the ionization potentials of chemical substances in the target. If the discrete energy levels of electrons bound in the target molecule are given by ϵ_i , an accurate expression of the integration in the above equation should be,

$$S = \frac{2\pi Z_1^2 e^4}{m_e v^2} N \sum_i n_i \ln \frac{2m_e v^2}{\epsilon_i}. \quad (28)$$

Now, the density of states for electrons in the target matter are high enough to average by numerical integration over the range of ε_i , and the summation can be parameterized by an averaged ionization potential of I as [20],

$$\frac{1}{Z_2} \sum_i n_i \ln \varepsilon_i = \ln I. \quad (29)$$

Then, S can be expressed with I as,

$$S = \frac{2\pi Z_1^2 e^4}{m_e v^2} N Z_2 \ln\left(\frac{2m_e v^2}{I}\right). \quad (30)$$

The direct energy transfer from the incident particle to the target matter below its ionization potentials can be calculated based on the total transition dipoles of the target molecular substances. The generalized oscillator strength ($f_n(Q)$) corresponding to a discrete energy level with a quantum number of n can be represented by $F_n(Q)$ as,

$$f_n(Q) = \frac{\varepsilon_n}{Q} |F_n(Q)|^2. \quad (31)$$

Here, the oscillator strength is defined as a function of transferred energy to the molecular substances (Q). Thus, the total energy loss by this scheme can be calculated by,

$$S = N \sum_n \int \varepsilon_n \frac{2\pi Z_1^2 e^4}{m_e v^2} \frac{dQ}{Q^2} |F_n(Q)|^2 = N \sum_n \int \frac{2\pi Z_1^2 e^4}{m_e v^2} f_n(Q) \frac{dQ}{Q}. \quad (32)$$

For f_n , it's summing up should be equal to the total number of electrons in the target, i.e., Fermi's golden rule. This can be simply represented by,

$$\sum f_n = Z_2, \quad (33)$$

and again the oscillator strength is correlated directly to I as,

$$\ln I = \sum_n f_n \ln \varepsilon_n. \quad (34)$$

Substituting Equation (34) into Equation (31), we obtain,

$$S = \frac{2\pi Z_1^2 e^4}{m_e v^2} N Z_2 \ln\left(\frac{2m_e v^2}{I}\right). \quad (35)$$

This shows a striking contrast to Equation (30), showing an equal contribution of energy transfer above and below I , the averaged ionization potential. Finally, the overall value of S can be,

$$S = \frac{4\pi Z_1^2 e^4}{m_e v^2} N Z_2 \ln\left(\frac{2m_e v^2}{I}\right). \quad (36)$$

Based on this equation, the spatial distribution of released energy by an incident particle is discussed in an isolated particle track.

Since the quantum mechanical description of electronic stopping was proposed for the first time by Bethe [10,11] in 1930's, a number of further theoretical approaches have been continuously discussed, aiming for a more precise estimation of stopping power within variable energy regimes of the incident charged particles. Particularly in the high-velocity regime (above 1 MeV/u), the relativistic effects were taken into accounts by Bloch [21], the shell correction and the density effect correction by Fano [22], and the effective charge correction by Bohr and Northcliff [23,24], respectively. In the

low-velocity regime (significantly below 1 MeV/u), nuclear stopping becomes predominant resulting in developments of the non-perturbative stopping models based on the electron exchange within the collision events by Firsov [25], the Thomas-Fermi model by Lindhard and Scharff [26], and the electron gas model by Fermi and Teller [27]. At the later stage of the collision cascades, a high energy charged particle penetrates the target with slowing down to as represented by T_{\min} in Equation (27). Here, the electronic stopping can no longer be derived from a series of separable binary collisions because of the complicated energy exchange between the particle and the target electrons, which is often referred to as “electron–phonon coupling”. Several theories have therefore been proposed, embedding new electronic and nuclear stopping mechanisms: two-temperature models [28], the Coulomb explosion model [29], and thermal spike model [30].

Overcoming these complexities due to variable velocity-dependent electronic stopping processes, quantum-mechanical descriptions by the use of first-principle calculations have attracted attention since the 1980s [31–34]. These approaches have striking advantages in terms of the non-empirical calculation of electronic stopping over a wide range of particle velocities, including the stopping power maximum. The rapid development of computational capabilities, such as peta-scale or exa-scale supercomputers, have also realized the direct simulation of the electron dynamics of the system incorporating the quantum-mechanical effects, which now allows us to estimate precisely the mean energy transfer within many-body and complicated molecules with time-dependent density functional theory (TDDFT) simulations. The protocols to assess the energy transfer are based on a simple scheme to predict the distinct initial and final states of the systems with Kohn–Sham orbitals as:

$$i\frac{\partial}{\partial t}\psi(\mathbf{r},t) = [\nabla^2 + V(N,\mathbf{r},t)]\psi(\mathbf{r},t), \quad (37)$$

and the dynamic potential of V has been simulated in every step with short enough time intervals. In the most recent cases, the steps were divided into 2 at, revealing gradual changes of the energy state of each target molecule [35]. In this regard, further detailed models were developed rapidly in sequence, taking self-consistent, non-perturbative, and time-lapse treatment of electron dynamics into account for metals [36–38], semiconductors [39,40], and biomolecules [41,42].

The origin of the organic molecules on Earth, eventually “D’où venons-nous?”, has been a long-lasting unsolved fundamental question and remains worth discussing to date. Since a model reported for the origin of biomolecular homochirality involving extraterrestrial source of circularly polarized light by Rubinstein et al. [43], the polarized UV light has been regarded as the likeliest and most powerful energy source to initiate an imbalance in the enantiomers of organic molecules both in space and on Earth. The scenario has been widely supported and developed by numerous experimental evidences [44,45]. In reality, enantiomeric excesses were actually induced in solid-state leucine samples by circularly polarized synchrotron radiation, simulating astronomical sources such as neutron stars/magnetic white dwarfs [46].

One of the other plausible scenarios is related to radiation-induced reactions in the context of X-, and γ -rays, high energy electrons/protons in solar radiations, and heavy charged particles from our galaxy: a full stream of ionizing radiations. Various organic molecules have been found in space. Even complex organic molecules were detected from the dusts blasted out from comets. It has been considered that small molecules such as H_2O , CO , and NH_3 frozen at the surface of interstellar dusts cause chemical reactions by cosmic radiation to generate organic molecules. A simulating experiment revealed that amino acids were generated by irradiating these small molecules with ultraviolet radiations at 12 K [47].

The other important and attractive topic yet unsolved is the origin of homochirality in the earth—why natural amino acids are the L-form while D-forms are enriched for sugars [48]. Since the enrichment of one isomer was found not only in the earth, but also in some meteorites [49], the cosmic scenario has been supported by many works, and may give a convincing answer to the origin of homochirality. In light of the higher angular momentum of non-spherical multi-atomic particles than

that of ultra-violet light or spin-polarized electrons, the particle induced intra-track chemical reactions will be a powerful candidate to lead an excess of one enantiomer, approaching the start of life.

2. Single Particle Nanofabrication Technique (SPNT) as a Versatile Tool for Nanofabrication

Ionizing radiations including high energy charged particles are ubiquitous in our daily life, particularly the later present in solar radiations. Quantitative analysis of the energy deposition by the ionizing radiations is crucial for sustainability of lives and materials, however the dosimetry of cosmic rays with a variety of particles and a broad energy spectrum have been challenging to date. Ionizing radiation met polymeric materials in the beginning of 20th century [50,51] as a powerful tool of functionalization by chemical reactions induced via reactive intermediates such as ions, ion radicals, and neutral radicals. The reactive intermediates, distributed homogeneously in the bulk polymeric materials, promote crosslinking, main chain scission, and subsequent graft polymerization reactions, which often dramatically improve the physical and mechanical properties of the polymeric materials [52]. Focusing on the functionalization of tons of polymeric materials, the primary choices of the ionizing radiations to lead the intermediates have been γ -rays and/or high energy electrons because of their high permeability into the materials with the lower S , securing the homogeneity of spatial distribution of the intermediates [53]. In contrast, a high energy heavy charged particle with higher orders of S has attracted much attention because of the intensive spatial distribution of the released energy, and hence the intermediates, leading to a unique chemical reaction which has never been realized in the context of bulk thermal/mechanical/photo-induced chemical reactions [54].

The severe damage to organic substances induced by the particle have been of particular interest to visualize the particle track in the materials for a long time as noted, and area of the latent tracks in the materials can be facilely etched, modified, and re-filled by the chemical protocols after irradiation [55]. The resulting nano/micro holes and beads provide unique nanospaces with an extremely high aspect ratio, and are developed as platforms for a variety of functional materials [56].

In view of the dosimetry of cosmic rays of high energy charged particles, several calculation codes such as CREME96 have been developed based on the numerical modelling of events caused by ionizing radiations to predict cosmic ray effects onto materials and devices in the last decade [57]. The rapid development of such calculation codes allows us to evaluate separately and precisely the effects of a variety of charged particles with a broad energy spectrum. An experimental approach to micro-dosimetry for a charged particle has been also investigated vigorously as seen in the "ion track membrane" works, where each latent track of a charged particle in a polymeric film could be etched chemically and visualized microscopically [58]. Numerous information concerning an incident charged particles such as momentum, charged state, and kinetic energy could be delivered by the size and direction of the visualized "nano holes".

Generally, the kinetic energy loss of the particle is negligible in a target of μm -thick organic polymer film for the heavy charged particle with tens MeV kinetic energy, preserving the linearity and uniformity of a latent track and the resulting "etched nanoholes". The engineering of the sizes and shapes of the "nano holes" has also been widely studied and developed by the subsequent chemical etching protocols to the latent track formation. The linearity of a "nano hole" reflects precisely the momentum of an incident particles, thus the network structure of the "nano hole" aggregates with controlled orientation can be applicable to form 3D holographic structures [59]. A simple approach to utilize "nano holes" is the formation of polymeric nano-porous membranes with selective ion transport and tuned permeability to the solutions. In the nano-porous membrane systems, the ion selectivity is engaged in interplay with the solvent permeability, and it is indispensable to tune the size and uniformity of the nano-pore precisely to overcome the above interplay and realize the sharp selectivity with high enough permeability [60]. The "nano holes" given by the high energy charged particles have been regarded as ideal platforms to solve the above issues in nano-porous membranes, of which application to those for fuel cells has been launched recently [61].

Functionalization of the “nano holes” has been of interest since the first discovery of particle tracks. The “nano holes” formed by the track etching could be worked as nano channels responding to external stimuli such as an electric field and/or ion (proton) strength (concentration) [62]. This type of responsive property could be applied to nanofluidic devices (diodes) to rectify the transport of ions [63]. The surfaces of the nano channels also have been functionalized by metal oxides [64], and the functionalized nanopores by thermo-responsive molecules have also been demonstrated as ion pumping channels [65]. The morphological change induced by “nano holes” is also crucial to control the surface properties of the membranes, for instance, the precise modulation of the optical reflectance could be obtained [66].

All these applications of the latent tracks given by the high energy charged particles are based on “damages” of molecular materials, and only few reports are on the materials fabrication such as target polymers/molecular materials. In many cases, physical/chemical properties of the latent tracks are missed and utilized simply as a platform for chemical reactions, leads to the formation of nanomaterials in the templated surface. The question is whether it is possible to produce nanomaterials confined in a nanospace of a particle track, retaining the physico-chemical properties of the target organic substances. The value of S of a high energy heavy charged particle often reaches up to 3–4 orders of magnitude higher than the conventional γ -rays and high energy electrons in organic substances with a typical gravitational density of 1 g cm^{-3} , but considering the efficiency of chemical reactions represented by G -values [67], the overall yield of chemical reactions is still insufficient to cause dynamic changes to the properties of molecular materials. This is the answer for the question that was initially encountered for radiation effecting the matter. Polymeric materials with long linear chain like structures exhibit exceptional physical/mechanical properties, known as “plastics”, and especially the rheological properties depend strongly on the chain length both in solutions and condensed phases [68]. Excellent theoretical formulations on the properties of polymeric materials have been successfully developed by Flory [69], deGennes [70,71], etc., suggesting the feasibility of a limited number of crosslinks/chain scissions in an isolated particle track, leading to nanomaterials formation along the particle trajectory [72].

To date, lithographic techniques are the primary choice to fabricate nanostructures based on organic substances, and most of the semiconductor devices are now patterned by replicating the structure of thin organic layers (resist materials in micro-nano lithography) where the nano-structures are formed via photo- or radiation- induced reactions in the layer [73]. In this context, the most important factor is the determining the size and its accuracy to generate patterns by the intensive deposition of the released energy from incident photons/particles, and precision optics and focusing systems are indispensable to confine the chemical reaction into nm-sized spaces. However, the intra-track reactions based on the released energy from an isolated single particle provides intrinsically an ultimate limit of the “intensive deposition” into real nm-sized cylindrical spaces, without using any optics and focusing systems.

The sizes of a particle track are defined precisely by the theoretically derived value of S for an incident particle with certain kinetic energy, and the dissipation process occurs by knocking out electrons through ionization events [74–77]. Here, we start from the equipartition theorem of energy released from a charged particle given by Equations (30) and (35), showing the inelastic collision processes, which can be divided into two kinds of collisions: indirect (ionizing) and direct energy transfer processes. The latter are often referred to as “knock-on” collision events, in contrast to the Coulombic force mediated interactions between the charges of an incident particle and electrons in the target media, which result in knocked-out secondary electrons, which is referred to as “glancing” collision events. Here, the value of S is dissipated equally to the processes, and the size of “knock-on” collision depends only on the velocity of an incident charged particle, defined as v_c . The upper limit (r_p) of the size of the “glancing” collision can be given by the highest energy of knocked-out electrons.

The spatial distributions are presumed to be constant for the former, and obey a conventional inverse square law for the latter as,

$$\rho_c = \frac{S}{2} [\pi r_c^2]^{-1} + \frac{S}{2} \left[2\pi r_c^2 \ln \left(\frac{e^{1/2} r_p}{r_c} \right) \right]^{-1} \quad (38)$$

and

$$\rho_p(r) = \frac{S}{2} \left[2\pi r^2 \ln \left(\frac{e^{1/2} r_p}{r_c} \right) \right]^{-1}, \quad (39)$$

where $\rho_c(r)$ and $\rho_p(r)$ are the distribution function of the released energy in two area, often called as “core” and “penumbra(halo)” areas. Evidently, the former is far higher than the latter in the orders, and typically $r_c \sim$ a few nm or less. The range of secondary electrons is 2–3 orders of magnitude larger than r_c , however for high energy heavy charged particles in non-relativity energy range, the value of $r_c \sim 100$ nm at the largest. In solid phase of organic substances, limited diffusive motion of chemical intermediates secure their spatial distribution roughly proportional to the initial energy distribution represented particularly Equation (39): and this is the largest limit of the sizes of reaction field, which is also suggestive of the field well confined into nm-sized cylindrical area.

In order to cause a significant mechanical/rheological change of polymeric materials within the area, it is necessary to estimate the criterion for the density of chemical reactions (chemical core). Assuming cross-linking reactions as a key to immobilize the molecules in the chemical core and produce nanogels, we can easily calculate the required density of energy to produce sufficient crosslinks for polymer gelation based on the value of crosslinking efficiency; $G(x)$. Generally, for gel formation in a polymer system, it is necessary to introduce one crosslink per polymer molecule. Assuming a sole contribution from the crosslinking reactions in the chemical core, the threshold density of ρ_{cr} is given by,

$$\rho_{cr} = \frac{100dA}{G(x)mN} \quad (40)$$

where A , d , m , and N are Avogadro's number, gravitational density of polymer solids, mass of monomer unit, and the degree of polymerization, respectively. By substituting $\rho_p(r)$ in Equation (39) with ρ_{cr} gives the following requirement for r as [78],

$$r^2 = \frac{S \cdot G(x)mN}{400\pi dA} \left[\ln \left(\frac{e^{1/2} r_p}{r_c} \right) \right]^{-1} \quad (41)$$

This gives a clear estimate of the chemical core size. If we employ a heavy particle with $S \sim 4000$ eV nm⁻¹ and chose the polymer target with $G(x) \sim 0.1$ (100 eV)⁻¹, $M_w \sim 10000$ g mol⁻¹, Equation (41) leads to an estimate of r as ~ 5 nm, which is competitive or even smaller than the typical sizes of nanostructures fabricated by present lithographic techniques. The sizes of the nanostructures fabricated by the present scheme, SPNT, are discussed quantitatively based on this theoretical aspect.

Crosslinking reactions confined in the above cylindrical area were successfully visualized for polysilanes upon irradiation to MeV order charged particles. The visualization could be done in the following simple steps: (1) irradiation of thin solid films of polysilanes of ~ 1 - μ m thickness where the energy loss of incident particle is negligible to the initial kinetic energy, (2) immersing in the solvent which can dissolve the polymers prior to crosslinking reactions, and (3) visualization by the cylindrical crosslinked nano-gels by atomic force microscopy (AFM). The images obtained by AFM are shown in Figure 1. The thickness of the nanowires changed significantly by the modulation of S of incident charged particles, which is clearly shown in the dependence of r on S as summarized in Table 1.

Table 1. Values of r observed in polysilane^a upon irradiation to various particles. Data quoted from ref. [78] ©2005, American Chemical Society.

Particles	Energy/MeV	S/eV nm ⁻¹	r /nm
¹ H ⁺	2.0	15	0.14
⁴ He ⁺	2.0	220	0.60
¹² C ⁺	0.50	410	1.1
¹² C ⁺	2.0	720	3.4
¹⁴ N ⁺	2.0	790	3.8
¹⁴ N ⁺	2.0	790	3.6
⁵⁶ Fe ²⁺	5.1	1550	5.5
²⁸ Si ²⁺	5.1	1620	5.9
²⁸ Si ⁵⁺	10.2	2150	6.1
⁴⁰ Ar ⁸⁺	175	2200	6.1
⁵⁶ Fe ⁴⁺	8.5	2250	5.8
⁵⁶ Fe ⁵⁺	10.2	2600	7.7
⁸⁴ Kr ²⁰⁺	520	4100	7.9

^a $M_n = 1.2\text{--}1.5 \times 10^4 \text{ kg mol}^{-1}$.

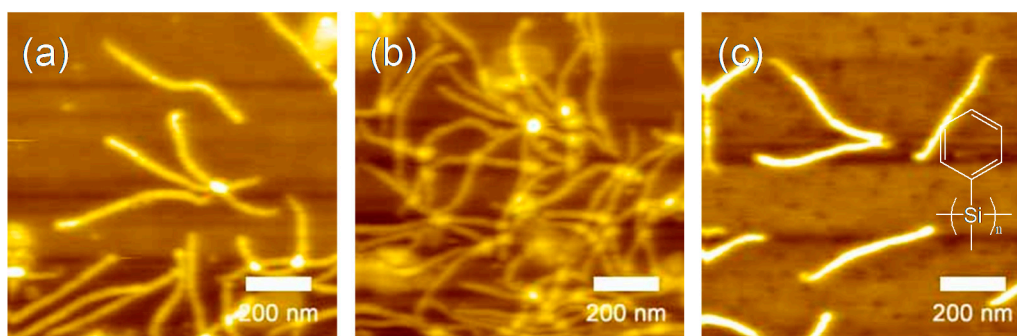


Figure 1. AFM micrographs of polysilane based nanowires. The nanowires were formed by 500 MeV ¹⁹⁷Au particle irradiation to (a,b) polysilane ($M_n = 1.2\text{--}1.5 \times 10^4 \text{ kg mol}^{-1}$) and (c) polysilane ($M_n = 3.3\text{--}6.8 \times 10^5 \text{ kg mol}^{-1}$) thin films at (a) 3.0×10^9 , (b) 5.0×10^9 , and (c) 1.0×10^9 particles cm^{-2} , respectively. The thickness of the target films were (a,b) 350 nm and (c) 250 nm. Reprinted with permission from ref. [79] ©2007, Nature Publishing Group.

Fine patterns of chemical cores in the AFM micrographs reveal clear 1D rod-like structures (nanowires) on the substrate. It should be noted that the density of the nanowires on the substrate increased clearly with an increase in the number of the incident particles, and the observed number density of the nanowires coincided with the number density of the incident particle. This is also suggestive that “one nanowire” is produced, corresponding incident particle along its trajectory, which is a clear evidence of the model described above. The length of the nanowires is uniform in each image, and is consistent precisely with the initial thickness of the film. This is due to the geometrical limitation of the distribution of crosslinking reaction: the gelation occurs from the top-surface to bottom of the polymer film. Thus, the length of the nanowires can be perfectly controlled by the present technique. Based on the measurement of cross-sectional trace of the nanowires by AFM, the radial distribution of crosslinks in the nanowires is discussed in terms of r , defined as the radius of the cross-section. This strongly supports the hypothesis of theoretical Equation (41), where the value of r is determined primarily by the molecular weight of the target polymer, the values of $G(x)$, and S .

Upon extension of the SPNT to a wider range of polymeric systems with a variety of backbone structures, some discrepancy was found between predicted and measured values of r respectively by Equation (41) and the direct AFM traces. For instance in case of polysilane, using the reported value of $G(x) = 0.12$ derived from radiation-induced changes in molecular weight, the values of r

calculated by Equation (41) were compared with the experimental values, showing a good consistency with the experimental values for polymers with sufficient chain length ($M_n > 10^4 \text{ kg mol}^{-1}$). However, a considerable discrepancy occurs between the calculated and experimental results for the polymer with shorter chain lengths.

The global configuration of the polymers depends heavily on the length of the polymer chains, leading to transformation from random coil (long chain) to rod-like (short chain) conformations. The gyration radius of a polymers, which determines the size of a polymer spreading in the media, is correlated with this transformation. The correlation function between R_g and N is provided by the well-established Flory–Huggins theory [80] as given in the following simple form,

$$R_g = \kappa M^{\nu}, \quad (42)$$

where κ is the Flory–Huggins parameter, M is the molecular weight of the polymer, and $\nu = (\alpha + 1)/3$. Based on the persistence length of the target polymer materials, the scaling law for a helical worm-like chain model results directly in an index α from Equation (42). Thus, the effective volume of a polymer chain can be simply calculated as $4/3\pi R_g^3$, and the substitution of mN/dA in Equation (41) with the effective volume leads the next final expression [78],

$$r^2 = \frac{S \cdot G(x) N^{3\alpha}}{400\pi\beta} \left[\ln \left(\frac{e^{1/2} r_p}{r_c} \right) \right]^{-1}, \quad (43)$$

where β is the effective density parameter of the monomer unit (kg m^{-3}). Based on Equation (43), the calculated value of r is plotted again the experimental values in Figure 2.

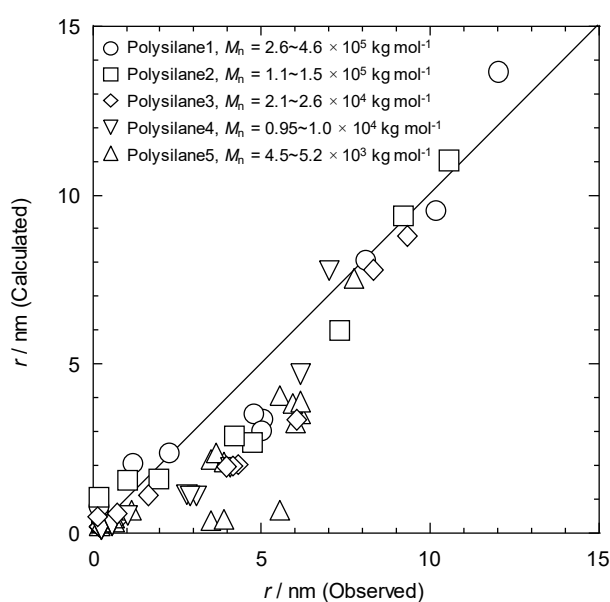


Figure 2. Correlation between r values estimated experimentally by gel traces or direct AFM measurement and the ones by theoretical calculations with Equation (43). Reproduced with permission from ref. [78] ©2005, American Chemical Society.

All the polymers with different molecular weights, follow a linear trend, and the calculated values display good correspondence in the range $r > 7 \text{ nm}$. The underestimated values of r by Equation (42) for $r < 7 \text{ nm}$ suggests that the initial deposition of energy and the radial dose distribution estimated by Equation (39), which do not account for the radial distribution of chemical intermediates and thus cannot model the concentration of crosslinking in the core of the ion track. The value of $G(x)$ increases dramatically with an increase in the density of reactive intermediates. Based on the assumption that

$G(x)$ is a function of the density of deposited energy, the present results indicate that the yield of the chemical reaction is dependent on the energy density. Cross-linking reactions in ion tracks therefore have potential for not only single particle fabrication with sub-nanometer-scale spatial resolution for any kind of cross-linking polymer, but also the study of nanoscale distributions of radial dose and chemical yield in an ion track.

The successful fit between the experimental values and Equation (42) is not perfectly matched since the values of r were determined experimentally in air by tracing the morphology of the nanowire surfaces by a scanning probe microscope, while the Equation (42) was derived directly from the solution-based theory of polymer backbone conformations represented by Equation (41). The deviation of the measured radii from the theoretical predictions stems from the theoretically neglected nanowires–solvent interactions during the isolation of the nanowires from the non-irradiated polymer. The so-called “development” isolation was carried out by the washing out of non-crosslinked polymer materials by a “rich” solvent that interacts not only with the pristine polymer, but also to the nanowires themselves. The nanowires also interact strongly with the surfaces during these procedures and the subsequent drying processes, and this is a case of the “memorized” shape of macromolecules in solution even at the air–substrate interfaces. The dominance of crosslinking reaction upon irradiation to the charged particle is the only prerequisite for the polymeric materials to give nanowires via intra-track reactions by SPNT. This simple requirement presents us with an extremely wide range of applicability of SPNT to construct 1D nanostructure formation based on a variety of polymeric materials.

2.1. 1D Nanostructures Based on a Variety of Polymers

SPNT is applicable to various synthetic polymers other than polysilanes. The key to afford insoluble 1D nanostructures is to realize sufficient crosslinking reaction efficiency, $G(x)$, that is mostly determined by chemical structures of polymers and energy/species of heavy ions. For example, polystyrene derivatives were extensively studied, and the formation of clear nanowires were confirmed after the development with aliphatic or aromatic hydrocarbon solvents [81,82]. Halogenated derivatives, poly(4-chlorostyrene) and poly(4-bromostyrene), were also irradiated with ^{129}Xe ion beams, giving thicker nanowires with larger cross-sectional diameters [83,84]. The possible reason for the increase in diameters of nanowires resulted not only from the molecular weight of initial polymers, but also the dissociative electron attachment reactions often observed for halogenated hydrocarbons [85,86]. Reactive chemical species such as radicals are generated with a higher rate, because the nucleophilic attack of secondary electrons to a halogenated core to release a halide ion and leave neutral radical. In the classical radiation chemical processes, one of the typical primary processes to lead stable neutral radicals is the dehalogenation reaction through electron dissociative attachments. This process could be implemented to a substituent of the representative crosslinking type polymers: poly(chlorostyrene)s. Upon irradiation with high energy charged particles, significant jump in the yield of neutral radicals was observed as well as the dehydrogenation reaction of α protons, resulting in increase in both of crosslinking efficiency and of the cross-sectional diameter. Conjugated polymers such as polyaniline (PANi) and poly(3-hexylthiophene) (P3HT) were also studied as starting materials for SPNT [87], where the absorption and photoluminescent spectra of the resulting nanowires are similar to those of the starting polymer films.

The capability of post-functionalization and post-treatment of nanowires is worth noting for the extension of the SPNT protocol. Polycarbosilane (PCS) is known as a precursor polymer for silicon carbide (SiC), a material with high mechanical properties and thermal conductivity, having chemical stability. Mechanical properties can be strengthened through the fiber-reinforced composite ceramics. To access fibrous SiC from PCS precursors, SPNT and following calcination process was demonstrated [88]. PCS nanowires were fabricated by 450 MeV ^{129}Xe beam irradiation to afford uniform nanowires with controlled number density. Then, pyrolysis was performed at 1000 °C under Ar atmosphere, resulting in SiC with the shrinkage of the nanowires. Considering the densities of PCS and SiC, the observed shrinkage of 33%–44% is reasonable for the conversion from PCS to SiC

nanowires. XRD analysis of the nanowires supported the formation of both α and β phases of SiC, which suggests the structural difference between core and penumbra regions.

Another feature of SPNT include block-*co*-nanowire formation by simply applying SPNT to multilayer films. By using hydrophobic/hydrophilic multilayer polymer films, the morphology control of segmented nanowires was reported [89]. In this work, PCS and poly(methylphenylsilane) (PMPS) were chosen as hydrophobic polymers while poly(hydroxystyrene) (PHS) was used as a hydrophilic one. PCS and PMPS are soluble in toluene but insoluble in isopropylalcohol (IPA), while PHS has the opposite solubility. This orthogonal solubility enables the preparation of multilayer films by a simple spin-coating method without affecting lower layers. PCS-PHS-PMPS films were irradiated with heavy ions and developed with toluene/IPA (2/1 v/v) mixtures. AFM observation disclosed that the obtained nanostructures adopt unique octopus-like morphology, where the central PHS segments selectively aggregate among adjacent nanowires (Figure 3). It is suggested that the bindings of the different polymer segments at their interfaces play an important role in the tangling of hydrophilic polymer segments with stretched hydrophobic polymer legs. The heteromolecular cross-linking reactions at the interfaces of PHS/PCS or PHS/PMPS would be key for the bindings of the multi-segment nanowires.

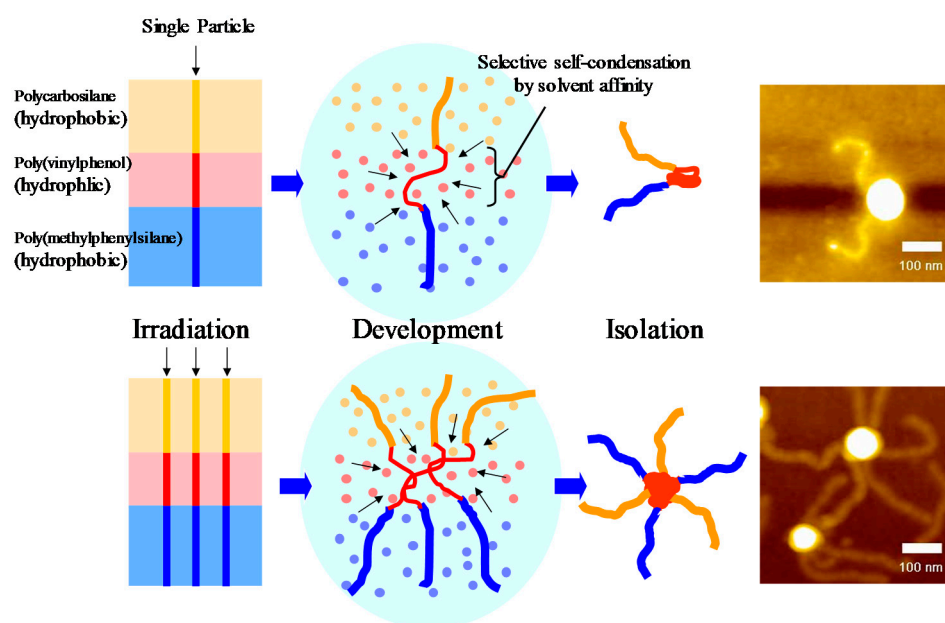


Figure 3. Selective self-entanglement of three-segment poly(methylphenylsilane)/poly(hydroxystyrene)/poly(carbosilane) nanowires prepared by exposure of the corresponding film to 454 MeV $^{129}\text{Xe}^{25+}$ ion beam at fluences of 1.1×10^9 (upper) and 5.3×10^9 ions cm^{-2} (lower). Reproduced with permission from ref. [89] ©2006, American Chemical Society.

2.2. 1D Nanostructures Responsive to External Stimuli

If the starting polymers exhibit changes in conformation upon applying the external stimulus (thermal- or photo- induced stimuli), the corresponding nanowires developed by SPNT should retain such responsiveness that can be visualized by microscopies as a nanoscale event. Poly(*N*-isopropylacrylamide) (PNIPAAm) is a famous thermoresponsive polymer having a lower critical solution temperature (LCST). This polymer is hydrated and swelled below 32 °C, but shrinks and finally segregated over that temperature by releasing the water molecules. The temperature-responsive swelling–shrinking behavior was clearly visualized in the form of nanowires. Although pure PNIPAAm films failed to form nanowires via 490 MeV $^{192}\text{Os}^{30+}$ ion beam and following development with IPA, the thick nanowires were successfully obtained from a hybrid film of PNIPAAm/*N,N'*-methylene-bis-acrylamide (MBAAm) cross-linker (100/20 wt/wt) [90]. After the resultant nanowires on substrates are placed in water at controlled temperatures, the nanowires shrank

under the conditions of 40 and 50 °C, whereas no distinct change was observed at 25 °C in water (Figure 4). From a more quantitative aspect, the increase in cross-sectional diameter and decrease in length were revealed in the PNIPAAm/MBAAm nanowire system. Nanowires fabricated by SPNT are insoluble nano-size gels. This work showed the temperature responsiveness of PNIPAM is preserved in the nanogel form. The temperature responsive was further controlled in a reversible way by PNIPAAm–poly(vinylpyrrolidone) (PVP) block nanowires where the latter as an internal standard [91]. Irresponsive nature of PVP segments against temperature modulation gave a clear contrast to the morphological changes of PNIPAAm segments, and the changes induced by LCST of the base polymer: PNIPAAm were confirmed to demonstrate high reversibility under the sequential cycles of temperature modulation. This is suggestive of the future application of the present combined nanowires acting as stimuli-responsive containers such as drug carriers.

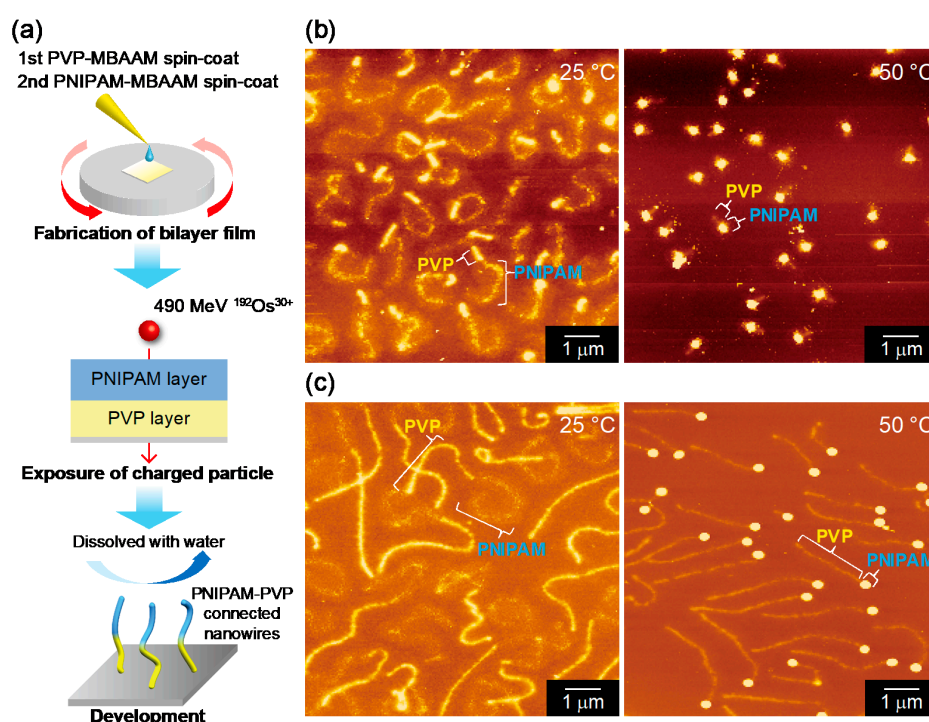


Figure 4. (a) Schematic representation of the formation of PNIPAM–PVP connected nanowires by SPNT from a PNIPAM layer (PNIPAM/MBAAM = 100/20) (upper) and a PVP layer (PNIPAM/MBAAM = 100/20) (lower) bilayer. (b,c) AFM topological image of PNIPAM–PVP connected nanowires with 0.1 and 0.5 μm thicknesses of PVP layer treated in water at 25 °C (left) and then 50 °C (right). PNIPAM–PVP connected nanowires were formed by irradiation of the bilayer films (b: PNIPAM layer/PVP layer = 0.5 μm/0.1 μm, c: PNIPAM layer/PVP layer = 0.5 μm/0.5 μm) with a 490 MeV $^{192}\text{Os}^{30+}$ beam at a fluence of $5.0 \times 10^7 \text{ cm}^{-2}$. Reproduced with permission from ref. [91] ©2015, American Chemical Society.

Photoresponsive properties were also imparted into nanowires by incorporating azobenzene moieties into the target polymers [92]. Azobenzene is a representative molecule undergoing a reversible photo-isomerization between its *-cis* and *-trans* isomers. Random copolymers of 9,9'-dioctylfluorene and 4,4'-azobenzene were prepared by Suzuki cross-coupling reactions. The electronic absorption spectral changes upon 401 nm light exposure were confirmed for the condensed phase. The copolymer films were successfully converted to nanowires by SPNT, and their photoresponsive property was directly investigated by morphological trace. Upon *trans*-to-*cis* isomerization, a clear transformation from a straight to wavy morphology was visualized, associated with an enhancement of roughness of the surface. Simultaneously, end-to-end distance of the nanowires increased with photoisomerization into *cis*-form. This implies that the microscopic isomerization in a molecular level could be reflected and scaled into the statistical changes of global configurations of the nanowires.

2.3. 1D Nanostructures with Optoelectronic Activities

The cross-sectional sizes of nanowires given by SPNT are ranging from few nm to . . . , suggesting their possible application as electronic conductive wires and/or platforms for quantum confinements of elemental excitation energies. The electrical conductivity of an isolated nanowire was measured by nano-gap devices with Pt electrodes [93]. Note that the electrodes were fabricated by a conventional electron-beam assisted lithographic technique followed by the vacuum deposition of Pt and lifting-off of resist materials used, and the nanowires produced by crosslinking reactions in polysilanes showed high enough tolerance for all the above processes, as seen in Figure 5. Current-voltage measurements of the nanowires bridged between the electrodes showed clearly the semi conductive nature of charge carriers, and a potential as electronic conductive nanowires.

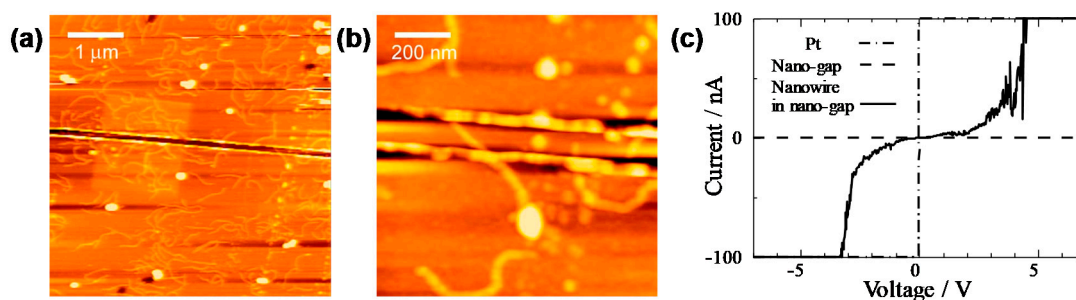


Figure 5. (a) AFM images of nanowires in the nanogap. (b) is an enlarged view of (a). (c) Current-voltage (I-V) characteristics of PMPS based nanowires between nanogap electrodes. The nanowires were formed by 500 MeV Au ion irradiation to polysilane thin film of 400 nm thickness. The fluence of ions was $1.0 \times 10^9 \text{ cm}^{-2}$. Reproduced with permission from ref. [93] ©2004, The Japan Society of Applied Physics.

The interplay of electronic and optical properties in isolated nanowires was examined for a series of conjugated polymers as the targets. Reflecting efficient radiative/non-radiative energy dissipation processes through the higher density of states in conjugated polymer main chains, the efficiency of main chain scission reactions is often suppressed, and surpassed by side chain crosslinking reactions. All conjugated polymers examined, namely Poly(9,9'-di-n-octylfluorene) (PFO), regioregular poly(3-hexylthiophene) (rrP3HT), and poly[2-methoxy-5-(2'-ethylhexyloxy)-ethylhexyloxy]-1,4-phenylenevinylene] (MEH-PPV), gave successfully corresponding nanowires with a high aspect ratio of ~ 200 , suggesting high enough mechanical strength without fragmentation during isolation (development) processes by solvents with high affinity for the initial polymer materials [94]. Particularly PFO-based nanowires exhibited clear signature of fluorescence from singlet excited state of PFO backbone conjugated systems with remarkably high quantum efficiency which was still observable for isolated nanowires on the substrates. The high quantum efficiency is also suggestive of disappearance of bulk quenching pathways for the excited states which had been often observed in condensed phase of luminescent organic materials.

“Intra-nanowire” Förster resonance energy transfer (FRET) from the energy harvesting nanowire body to tetramethylrhodamine (TAMRA) was demonstrated using fluorescent nanowires based on poly(9,9'-dialkylfluorene)s [95]. Random copolymers of (9,9'-dioctylfluorene) and (9,9'-di(5-hexynyl)fluorene) carrying terminal alkyne groups was synthesized. After formation of nanowires by SPNT, blue fluorescence from polyfluorene backbone was confirmed. TAMRA was attached by post-functionalization of the terminal alkyne groups via “click” chemistry on the surface of nanowire. After TAMRA-functionalization, fluorescence from the nanowires was turned into red as evident from confocal fluorescence microscopy, which indicates efficient FRET from polyfluorene-based nanowire body to TAMRA as schematized in Figure 6. Although this case reports the covalent conjugation between the nanowire surface and analyte (=TAMRA), the concept can be extended to the noncovalent interaction-based sensing systems with the extremely wide surface area of nanowires.

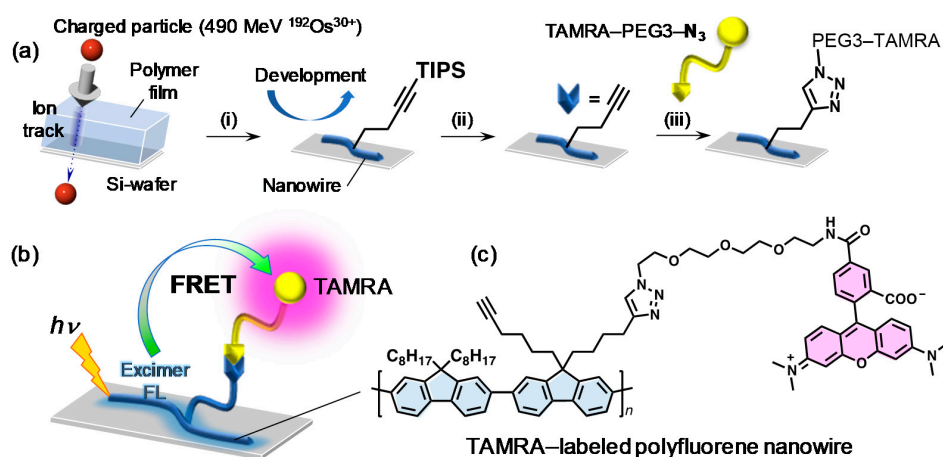


Figure 6. (a) Schematic illustrations of 5(6)-Carboxytetramethylrhodamine(TAMRA)-labeled polyfluorene nanowire fabrication by the SPNT: (i) High-energy charged particles induce nonhomogeneous cross-linking reactions along the “single” particle trajectories in a polymer film. The area unexposed to charged particles are subsequently developed with appropriate solvent, the remaining cross-linked sections then transform into nanowires with one end bound to the Si-wafer surface; (ii) Deprotection of TIPS-acetylenes with TBAF to give alkyne ($-\text{C}\equiv\text{CH}$) groups; (iii) Nanowire surface functionalization via copper-catalyzed alkyne-azide click reaction. (b) Schematic function of the FRET-based nanowire platform. (c) Chemical structure of the TAMRA-labeled polyfluorene nanowire. Reproduced with permission from ref. [95] ©2016, American Chemical Society.

2.4. 1D Nanostructures from Biomacromolecules

Inspired by the successful formation of stimuli-responsive nanomaterials and facile combination/joint of nanowire segments, SPNT has been extended to bio-macromolecules towards the future diagnostic/therapeutic/medical application of the nanowires. The first example of bio-macromolecular nanowires was given based on proteins [96]. Figure 7 shows bovine serum albumin-based nanowires isolated and visualized clearly by AFM. Crosslinking efficiency in protein molecules strongly depends on the composition/arrangement of amino acid in their chains, and albumin revealed to be an ideal platform to give nanowires through SPNT protocols. The length of the nanowires reached over 10 μm with extremely high aspect ratio of ~ 1000 . The presumed high mechanical strength from the aspect ratio could be ascribed to the competitive/higher density of crosslinks in protein nanowires. The high inter- and intra-chain reactions of amino acids arranged in albumin, allowing us the further functionalization of the nanowire surfaces. The dense distribution of amine groups on the nanowire surfaces could be biotinylated, and through biotin-streptavidine interactions, a variety of biologically active groups can be decorated on the surface of nanowire. It is noteworthy to mention that protein nanowires were digested by enzymes such as trypsin, suggesting principally that the nanowires are composed of peptide linkages.

Facile surface modification of nanowires allows us to impart biocompatibility to nanowires of commercially available polymers with the higher mechanical and/or optoelectronic properties. For instance, the surface of polystyrene nanowires could be activated through copolymerization of styrene with ethynylstyrene as represented in Figure 8, and grafting protocol using Click chemistry was applied to introduce terminal alkyne functional groups [97]. Antigen-antibody interactions, as in the above case, were well demonstrated to decorate the nanowires surfaces by bio-compatible molecules and macromolecules, such as proteins.

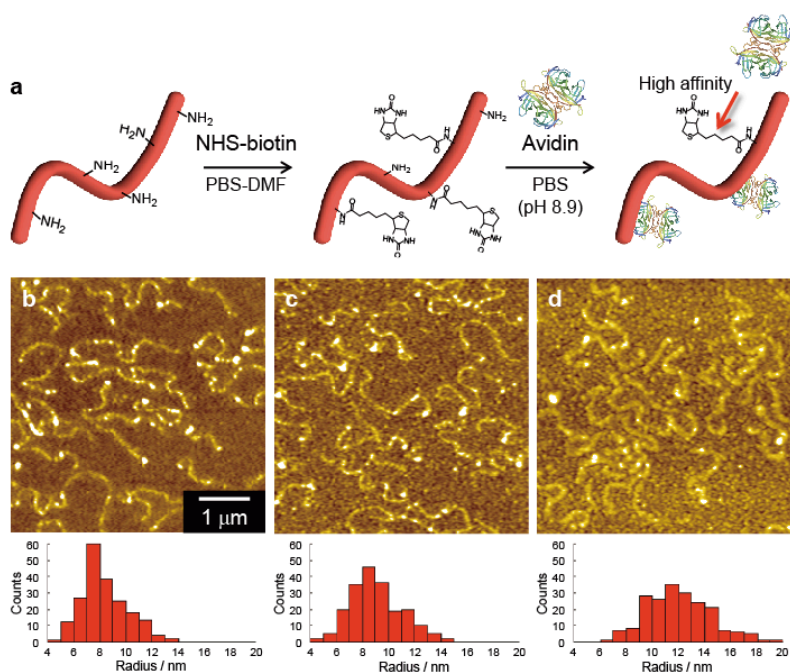


Figure 7. (a) Scheme showing the surface modification of HSA nanowires by introducing biotinyl groups and the affinity between biotinylated HSA nanowires and avidin. AFM images and radius distributions of (b) HSA nanowires, (c) biotinylated HSA nanowires, and (d) biotinylated HSA nanowires after immersion in an avidin solution at room temperature for 30 min. Reproduced with permission from ref. [96] ©2014, Nature Publishing Group.

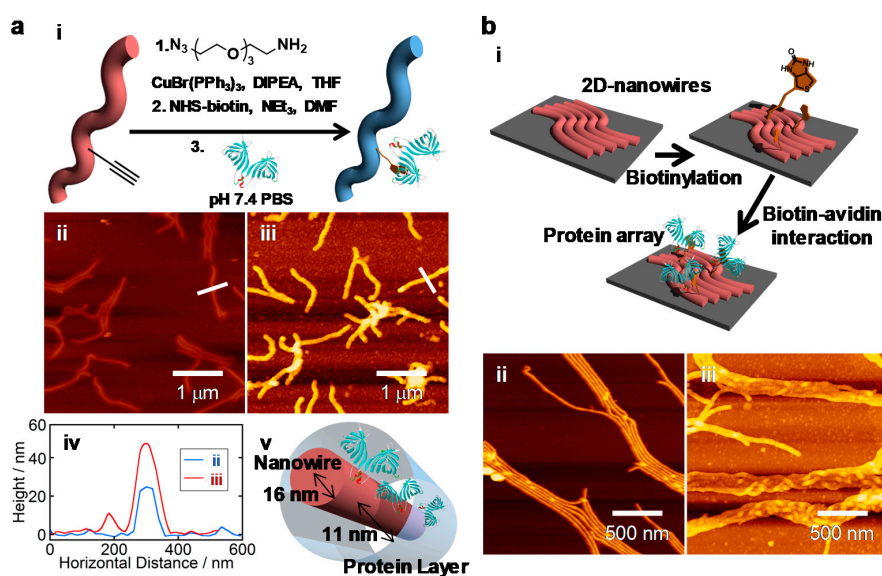


Figure 8. (a-i) Scheme for fabrication of the protein nanowires by using chemical modification and the avidin–biotin system. (a-ii) AFM micrograph of nanowires based on a PSES film prepared by exposure to 490 MeV $^{192}\text{Os}^{30+}$ particles at 1.0×10^8 ions cm^{-2} . (a-iii) AFM micrograph of modified nanowires. The surfaces were modified with avidin. (a-iv) Cross-sectional profiles of nanowires based on PSES before and after modification. (a-v) A visualization of a biomacromolecular nanowire covered with avidin. (b-i) Scheme for fabrication of the 2D protein sheets by modifying the assembly structure of the nanowires. (b-ii) AFM micrograph of arrays of nanowires prepared by exposing PSES film to 490 MeV $^{192}\text{Os}^{30+}$ particles at 1.0×10^8 ions cm^{-2} . Development was carried out in toluene for 5 min. (b-iii) AFM micrograph of arrays of protein-modified nanowires. The surface was modified with avidin. Reproduced with permission from ref. [97] ©2012, American Chemical Society.

Another challenging target is “sugar” to give nanowires by SPNT [98]. As revealed previously, an efficient DNA damage can be done by radiations in cancer radio therapy. Polysaccharides suffer significantly from main chain scission reactions, which make it challenging to promote crosslinking reactions in these materials. The primary process of the reaction was known to be triggered by the deprotonation reaction of hydroxy groups in sugar molecules, thus methylated polysaccharides were employed and led into nanowires successfully. Although fragmentation occurred relatively in the higher ratio, this was due to the lower crosslinking density.

2.5. 1D Nanostructure Formation for Visualization of Ion Tracks

One of the major/most critical issues in SPNT is spatial resolution/position sensitivity of “single” particle competitive to the size of nanowires. As demonstrated in the dosimetry of galactic cosmic rays in Section 2, the hitting position by a particle could be visualized clearly by subsequent chemical etching processes. However, the decomposition of the target organic substances simultaneously spoils the spatial resolution of an exact center of hitting position due to inhomogeneity/fluctuation of chemical reactions in the slow-wet processes. The direct visualization of the “latent” particle tracks was realized by a simple protocol: exposure to a humid environment soon after the irradiation of high energy charged particles [99]. Intra-track chemical reactions caused dramatic changes in the diffusion constant for small molecules, and herein water molecules penetrating selectively in the latent track led to a significant volume expansion only in the latent track area. Morphological traces on the surface allows for the precise determination of the hitting position of each charge particle with less than a few nm spatial resolution.

3. Single Particle Triggered Linear Polymerization (STLiP): Facile and Universal Polymerization Confined into nm-scaled Area

Macromolecules become insoluble with several crosslinking points, which makes them advantageous as starting materials for SPNT. Also, polymer materials are beneficiary due to easy film-formation capability. In contrast, small molecular materials require not only crosslinking but also chain-like polymerization reactions in order to afford insoluble nanogels. In addition, small molecules often cause crystallization that is sometimes disadvantage for film preparation. However, by the recent examinations using particular molecular design and solvent for development, small molecular materials have now been suitable candidate for ion beam triggered nanostructure formation. The method using small molecules was distinguished from SPNT and thus named as “single particle triggered linear polymerization (STLiP)”.

Silsesquioxanes are small molecular analogues of polysiloxanes and have amorphous nature to yield smooth films by spin-coating. Films of two silsesquioxane derivatives were exposed to 450 MeV ^{129}Xe beams, and uniform nanowires were obtained [100]. By comparing the two derivatives, the derivative carrying vinyl termini resulted nanowires with a large cross-sectional radius ($r = 10.1$) than that of the hydroxy-terminated derivative ($r = 7.0$ nm). Therefore, vinyl groups may be the key to efficient radiation-induced chemical reactions [83]. The information worth noting that includes the larger cross-sectional radius of the resultant nanowires from poly(silsesquioxanes) ($r = 14.3$ nm) than those from monomeric silsesquioxanes ($r = 10.1$ nm). This fact is reasonable, considering the size of the initial molecules.

Not only vinyl, but also other unsaturated bonds were found to be effective starting materials for STLiP method. Pentacene derivatives, 6,13-bis(triethylsilylethynyl)pentacene and 6,13-bis((triisopropylsilyl)ethynyl)pentacene were successfully converted to nanowires by the irradiation with 490 MeV ^{192}Os and developed with *n*-hexane [101]. The absence of nanowires from simple pristine pentacene implied the importance of unsaturated bonds, inner alkyne groups. One of the ultimately unsaturated carbon allotropes is fullerene derivatives. In fact, polymerization of C_{60} films by UV light [102] or electron beam [103], and their enhanced electrical conductivity [104] were reported previously. Furthermore, intra-track polymerization was also achieved by irradiation

with swift heavy ions at the fluence of $1 \times 10^{12} \text{ cm}^{-2}$ [105]. Although isolation of polymerized carbon nanowires has not been done, the track-shaped 1D nanostructures were evidenced by conducting-mode AFM measurements [106–108]. The isolation of fullerene derivatives nanowires was reported by Seki et al. [109]. Figure 9 shows a clear rod-like shape of nanowire as well as high resolution image of a nanowire representing polymerized fullerene molecules by irradiation with high energy heavy ions. The fullerene-based nanowires were incorporated in the active layer of P3HT/PCBM in photovoltaic devices. The role of unsaturated carbon–carbon bonds on the efficient nanowire formation by swift heavy ion irradiations could be explained on the basis of bond energy. The bond energy of a C–H bond is higher than that of C–C, C=C, and C≡C bonds, and the cleavage of a C–H bond releases a hydrogen radical or proton that is soon removed from the system. On the other hand, the cleavage of a carbon–carbon bond generates reactive radical species capable of polymerizations. The absence of terminal C–H— and the presence of unsaturated bond—may be the key for high reactivity upon irradiations. This hypothesis is related to the notion of hydrogen loss energy [110].

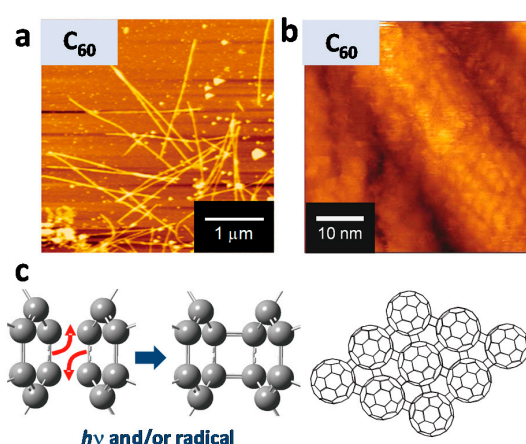


Figure 9. (a) AFM image of long and straight C₆₀ nanowires. (b) STM image of C₆₀ nanowires. (c) Proposed dimerization reaction via 2+2 cycloaddition. The right schematic shows the expected structure of the polymerized fullerenes. Reproduced with permission from ref. [109] ©2012, Nature Publishing Group.

Aromatic amines are the candidates for the starting materials of STLiP technique. Motivated by the easy radical cation formation of aromatic amines [111], STLiP was demonstrated for amorphous solid films of a series of aromatic amines [112]. The distribution of the cross-sectional radii of the nanowires is small that reflecting the size of the molecules, which is also discussed in the field of resist materials for lithography [113]. Pristine nanowires were obtained by irradiation with high energy heavy ions and following solvent treatment with aliphatic hydrocarbon solvents such as hexane and cyclohexane. When the isolated nanowires were immersed in CHCl₃, time-dependent fragmentation of the nanowires were monitored (Figure 10). This observation suggested that that the nanowires were formed not only by crosslinking (complete covalent bondings) but also by entanglement (multiple noncovalent interactions) of the polymerized products.

Further analyses from the mechanistic and quantitative aspects were performed by employing 9,9'-spirobi[9H-fluorene] (SBF) and its brominated derivatives [114]. Spin-coated films of SBF, 2-bromo-SBF (2Br-SBF), 4-bromo-SBF (4Br-SBF), 2,2'-dibromo-SBF (2,2'Br₂-SBF), 2,7-dibromo-SBF (2,7Br₂-SBF), 2,2',7,7'-tetrabromo-SBF (Br₄-SBF), 2,2''-bi-9,9'-spirobi[9H-fluorene] (SBF₂), and 2,2''':7''',2''''-ter-9,9'-spirobi[9H-fluorene] (SBF₃) were irradiated with 350 MeV ¹²⁹Xe²⁶⁺ ions, and their nanowires were isolated after development with toluene. Figure 11 shows a series of AFM micrographs visualizing the SBF-based nanowires with a variety of thickness and length, and apparently the thinner nanowires from SBF, 2,7Br₂-SBF, and 2Br-SBF suffered significant fragmentation during development processes under the strong solvent: toluene.

The r values were evaluated by cross-sectional views in AFM, revealing the order of $r(\text{SBF}) < r(\text{SBF}_2) < r(\text{SBF}_3)$ and $r(\text{SBF}) < r(2,7\text{Br}_2\text{-SBF}) < r(2\text{Br-SBF}) \sim r(4\text{Br-SBF}) < r(2,2'\text{Br}_2\text{-SBF}) < r(\text{Br}_4\text{-SBF})$. The order of the former can be interpreted as the effect of molecular size on the oligomerization/crosslinking reactions; the starting larger oligomers reach the polymerized products more easily. Larger r observed in Br-substituted SBFs reflects the dissociative electron attachment of the generated secondary electrons to the halogenated compounds and preferential cleavage of $\text{C}_6\text{H}_5\text{-Br}$ due to its smaller bond energy (~ 336 kJ mol $^{-1}$) than that of $\text{C}_6\text{H}_5\text{-H}$ (~ 472 kJ mol $^{-1}$). This explanation is supported by X-ray photoelectron spectroscopy (XPS) measurements, suggesting a significant reduction of the photoelectron signals, and hence composition, of Br atoms in the nanowires.

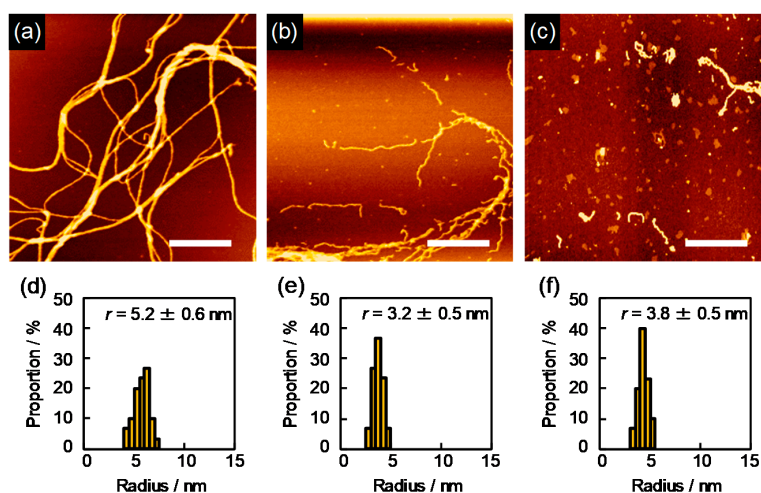


Figure 10. (a–c) AFM topographic images and (d–f) the radius distributions of the nanowires from a drop-cast film of 1, 3, 5-tris[(3-methylphenyl)phenylamino]benzene isolated via sequential development. The film was irradiated with 490 MeV $^{192}\text{Os}^{30+}$ ions at the fluence of 2.0×10^8 cm $^{-2}$ and developed by (a,d) *n*-hexane at 60 °C, followed by (b,e) CHCl_3 for 10 s and then (c,f) CHCl_3 for 2 min. Scale bars represent 500 nm. Reproduced with permission from ref. [112] ©2016, Royal Society of Chemistry.

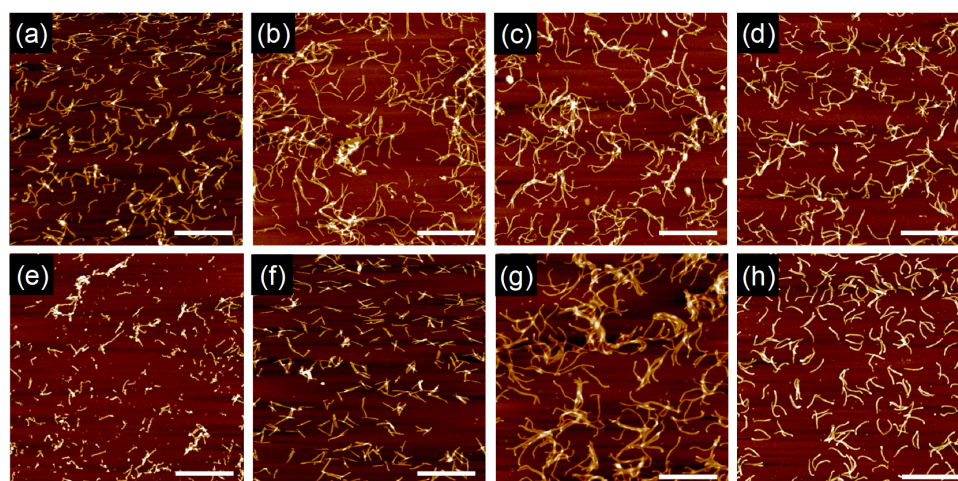


Figure 11. AFM topographic images of nanowires from dropcast films of (a) SBF, (b) 2Br-SBF, (c) 4Br-SBF, (d) 2,2'Br $_2$ -SBF, (e) 2,7Br $_2$ -SBF, (f) Br $_4$ -SBF, (g) SBF $_2$, and (h) SBF $_3$. The films were irradiated by 350 MeV $^{129}\text{Xe}^{26+}$ particles at a fluence of 1.0×10^{10} cm $^{-2}$ and developed by toluene at room temperature. Scale bars represent 500 nm. Reproduced with permission from ref. [114] ©2019, American Chemical Society.

Based on Equation (39), the energy density at the surface of nanowires ($\rho_p(r = r_{\text{obs}})$) was calculated as summarized in Table 2, by using the averaged cross-sectional radius of nanowires for each starting compound and the stopping power simulated by Monte-Carlo code (SRIM2008). The given energy per molecule around the nanowire surface (E_{molecule}) is also summarized in Table 2. These values were calculated from $\rho_p(r = r_{\text{obs}})$ and molecular volumes estimated from the crystal structures of the SBF derivatives. Most likely at the nanowire surface, at least one chemical bond is formed to immobilize the molecule. The reported crystal structures denoted that one SBF molecule is surrounded by six nearest neighbor molecules capable of bond formation, and the SBF molecule at the nanowire surface should react with either of the three inner molecules, in order to immobilized to a nanowire. Consequently, the G values for bond formation with the inner nearest neighbors are roughly estimated to be in the range of 8.6–9.7 (100 eV)⁻¹ for the monomeric SBF derivatives in this irradiation condition, whereas the dimer and trimer yielded smaller G values of 5.4 and 3.9 (100 eV)⁻¹, respectively. These values are larger than that for the case of polymers, revealing efficient solid-state polymerization of the SBF derivatives upon high-energy particle irradiation. Although this analysis does not take account competitive bond cleavages by irradiations, the solid-state intra-track polymerization reaction efficiency, G , was estimated for the first time to address the feasibility of organic molecules for the STLiP technique, leading to corresponding 1-D nanomaterials.

Table 2. Summary of density, calculated maximum radial range r_c and r_p , calculated electronic stopping power (S), radii in nanowire form r_{obs} , calculated energy density at the nanowire radii $\rho_p(r = r_{\text{obs}})$, estimated molecular volume V_{molecule} , given energy per molecule by high-energy ions E_{molecule} , and estimated G for SBF, 2Br-SBF, 2,2'-Br-SBF, Br₄-SBF, SBF₂, and SBF₃ upon irradiation with 350 MeV ¹²⁹Xe²⁶⁺. Data are quoted from ref. [114] ©2019, American Chemical Society.

	Density/g cm ⁻³	S/eV nm ⁻¹	r_c /nm	r_p /nm	r_{obs} /nm	$\rho_p(r = r_{\text{obs}})$ /eV nm ⁻³	$V_{\text{molecule}}/\text{nm}^3$	$E_{\text{molecule}}/\text{eV}$	$G/(100$ eV) ⁻¹
SBF	1.25 ^a	11,500	0.77	296	3.93	9.18	0.42	3.86	8.6
2Br-SBF	1.48 ^b	12,000	0.77	250	4.47	7.61	0.45	3.42	9.7
2,2'-Br₂-SBF	1.63 ^a	12,000	0.79	227	4.56	7.45	0.48	3.57	9.3
Br₄-SBF	1.84 ^a	12,000	0.83	201	4.81	6.90	0.54	3.72	9.0
SBF₂	1.34 ^a	12,000	0.75	276	4.35	7.87	0.78	6.14	5.4
SBF₃	1.24 ^a	11,000	0.78	298	4.48	6.76	1.27	8.58	3.9

^a Presumed from reported crystalline structures. ^b Speculated.

Sublimation is one of the remarkable characters for small molecules. The nanowires fabricated via SPNT or STLiP are always isolated by the development process. Development with organic solvents is an easy method that accelerates the throughput of various nanowires from variety of materials. At the same time, the isolated nanowires are always parallel to substrates due to the tensile force of solvent liquid and irreversible adhesion to the substrate. As an orthogonal isolation process toward development, sublimation has been tried recently. For example, vapor-deposited smooth films of C₆₀ were irradiated with high energy heavy ions at relatively high fluence (>10¹¹ cm⁻²) to form nanowires perpendicular to the substrate. When the film was developed with 1,2-dichlorobenzene, bundled nanowires were lying down to the substrate. In contrast, subsequent sublimation after irradiation afforded a different morphology. AFM measurements unveiled that the C₆₀-based nanowires were vertically oriented to the substrate, and the length of the nanowires correspond to the initial thickness of the films (Figure 12). The sublimation process is an alternative way to development, which opens another possibility for the orientation control of the nanowires developed by STLiP.

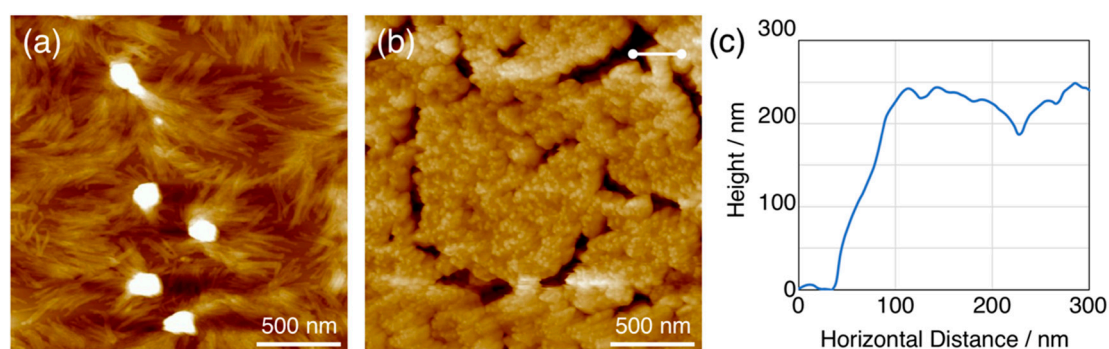


Figure 12. AFM images of nanowires from C_{60} after 490 MeV ^{192}Os irradiation at 10^{11} cm^{-2} and subsequent (a) development with 1,2-dichlorobenzene or (b) sublimation. (c) Height profile along white line indicated in (b).

4. Discussion

SPNT as well as STLiP techniques have been developed and demonstrated as unique and versatile methods to provide nanomaterials based on organic molecular systems where the sizes of the materials have been precisely controlled in a regime of a few nm with uniform distribution. However, the number density of fabricated nanowires in our techniques might be little small considering implementation to industrial scale because higher fluence irradiation make overlaps of ion tracks resulting in an obstacle to fabricate discrete nanowires. In terms of Poisson distribution, although ion beams at the fluence of 10^{11} cm^{-2} give about 2.5% overlaps, which can be the maximum irradiation density, the irradiation time for each sample should be relatively short. Thus, the automation of sample loading has good prospects for high-throughput preparation. While SPNT/STLiP techniques basically use a single particle aiming to control and/or minimize the size of nanostructures, unlike general ionizing radiation such as electron beams and X-rays, “single particle” does not mean “single atom” as a chemical reaction source to lead nanomaterials. We can substantially, for example, use an accelerated atom cluster bounded by chemical bonds as a reaction source. In this case, it can be possible that imparted energy in intra-molecule degrees of freedom of a cluster particle trigger chemical reactions and controlling dynamics of a single cluster break the symmetry of subsequently formed materials. It is also presumed that cluster ion beam can visualize that kind of symmetry breaking based on the visualization of organic materials by single-ion beams. For instance, this can be demonstrated by investigation of chirality of fabricated nanowires, that is, measurement of optical properties as an index of symmetry breaking, like circular dichroism (CD) and circularly polarized luminescence (CPL). These measurements however require an adequate amount of analyte for detectable outputs and are unsuitable for chiral evaluation of our nanowires. Therefore, some other experiments are hopeful candidates for the demonstration of symmetry breaking: incorporating nanowires into electronic devices as a chiral sensing, and morphology deformation of isolated nanowires by complementary interactions between chiral molecules. Furthermore, comparing reaction phenomena between single ions and cluster ions, it might be opportune to visualize the effects of rotary anisotropy of ion beams.

5. Conclusions

The dimension of nanostructures, nanomaterials, and nanodevices has been scaling down day-by-day since the second half of the last century, concurrently to the development of electronic integrated circuits. Now, the dimension is approaching the size equivalent to that of small organic molecules. Chemical reactions within the dimension induced by ionizing radiations have always played a crucial role in the determination of the sizes as well as their accuracy. A “single particle” provides an ultimate limit of the spatial distribution (chemical reaction field) as the energy source, and herein the successful nanomaterials fabrication is discussed and reviewed through the energy released within the field. Starting from the visualization of latent tracks formed by high energy charged

particles given by nuclear reactions, a variety of applications as well as the direct formation of the materials have been developed, with advantages of employed widely used nanofabrication techniques, particularly in semiconductor industries as follows: (1) intrinsically small special size of chemical reaction fields, (2) extremely high aspect ratio of the field reflecting intrinsic “indivisible” nature of single particle, and (3) facile way to combine a variety of nanomaterials. Considering the ubiquitous nature of high energy charged particles outside of our Earth, understanding the total landscape of high energy particle induced reactions will be critical to the origin of organic molecules, and provide the scenario for the origin of the breaking symmetry in our lives.

Author Contributions: Conceptualization of this article, S.S.(Shu Seki); methodology, S.S. (Shugo Sakaguchi) and K.K.; investigation, S.S. (Shugo Sakaguchi) and K.K.; resources, S.S. (Shugo Sakaguchi), K.K., S.S. (Shu Seki) and T.S.; data curation, S.S. (Shugo Sakaguchi), K.K., T.S.; writing—original draft preparation, S.S. (Shugo Sakaguchi), K.K., T.S. and S.S. (Shu Seki); writing—review and editing, S.S.(Shu Seki); visualization, S.S.(Shugo Sakaguchi) and K.K.; supervision, S.S. (Shu Seki).; project administration, S.S. (Shu Seki).; funding acquisition, S.S.(Shu Seki). All authors have read and agreed to the published version of the manuscript.

Funding: This work was partly funded by a Grant-in-Aid for Scientific Research (A) (26249145 and 18 H03918) and (B) (19 KK0134) from the Japan Society for the Promotion of Science (JSPS), and research grants from the Sekisui Chemical Grant Program and the Ogasawara Foundation for the Promotion of Science & Engineering.

Acknowledgments: This work was performed by use of high energy charged particle accelerator setups at Takasaki Advanced Radiation Research Institute, National Institutes for Quantum and Radiological Science and Technology (QST), Japan, under Facility Shearing Program and the Inter-University Program for the Joint Use of JAEA/QST Facilities, and at Inter-University Accelerator Centre, New Delhi, India.

Conflicts of Interest: The authors declare no conflict of interest.

References

1. Gieger, H.; Marsden, E. On a Diffuse Reflection of the α -Particles. *Proc. Roy. Soc.* **1909**, *82*, 495.
2. Rutherford, E. The Scattering of α and β Particles by Matter and the Structure of the Atom. *Philos. Mag.* **1911**, *21*, 669. [[CrossRef](#)]
3. Darwin, C.G. A Theory of the Absorption and Scattering of the Rays. *Philos. Mag.* **1912**, *13*, 901–920. [[CrossRef](#)]
4. Thomson, J.J. Ionization by Moving Electrified Particles. *Philos. Mag.* **1912**, *6–23*, 449–457. [[CrossRef](#)]
5. Bohr, N. On the Theory of the Decrease of Velocity of Moving Electrified Particles on passing through Matter. *Philos. Mag.* **1913**, *25*, 10–31. [[CrossRef](#)]
6. Bohr, N. On the Decrease of Velocity of Swiftly Moving Electrified Particles in passing through Matter. *Philos. Mag.* **1915**, *30*, 581–612. [[CrossRef](#)]
7. Seki, S.; Yoshida, Y.; Tagawa, S.; Asai, K. Electronic Structure of Radical Anions and Cations of Polysilanes with Structural Defects. *Macromolecules* **1999**, *32*, 1080–1086. [[CrossRef](#)]
8. Kobayashi, K.; Tagawa, S. Direct Observation of Guanine Radical Cation Deprotonation in Duplex DNA Using Pulse Radiolysis. *J. Am. Chem. Soc.* **2003**, *125*, 10213–10218. [[CrossRef](#)] [[PubMed](#)]
9. Wilson, C.T.R. Investigations on X-Rays and β -Rays by the Cloud Method. Part 2.— β -Rays. *Proc. Roy. Soc. A* **1923**, *104*, 192–212.
10. Bethe, H. Zur Theorie des Durchgangs schneller Korpuskularstrahlen durch Materie. *Ann. Phys.* **1930**, *5*, 325–400. [[CrossRef](#)]
11. Bethe, H. Bremsformel für Elektronen relativistischer Geschwindigkeit. *Z. Phys.* **1932**, *76*, 293–299. [[CrossRef](#)]
12. Seki, S.; Sakurai, T.; Omichi, M.; Saeki, A.; Sakamaki, D. *High Energy Charged Particle: Their Chemistry and Use as Versatile Tools for Nanofabrication*; Springer: London, UK, 2015.
13. Geiger, H. On the scattering of the α -particles by matter. *Proc. Roy. Soc. A* **1908**, *81*, 174.
14. Kittel, C. *Quantum Theory of Solids*; John Wiley & Sons Inc.: New York, NY, USA, 1963.
15. Lippmann, B.A.; Schwinger, J. Variational Principles for Scattering Processes. I. *Phys. Rev.* **1950**, *79*, 469–480. [[CrossRef](#)]
16. Born, M. Quantenmechanik der Stoßvorgänge. *Z. Phys.* **1926**, *38*, 803–827. [[CrossRef](#)]
17. Fano, U. Ionizing Collisions of Very Fast Particles and the Dipole Strength of Optical Transitions. *Phys. Rev.* **1954**, *95*, 1198. [[CrossRef](#)]

18. Fano, U. Penetration of Protons, Alpha Particles, and Mesons. *Ann. Rev. Nucl. Sci.* **1963**, *13*, 1–66. [[CrossRef](#)]
19. Mott, N.F.; Massey, H.S.W. *The Theory of Atomic Collisions*, 3rd ed.; Oxford University Press: Oxford, MS, USA, 1965.
20. Bohr, N.; Dan, K. *Atomic Interaction in Penetration Phenomena*; Munksgaard: Copenhagen, Denmark, 1948; Volume 18, pp. 1–144.
21. Bloch, F. Zur Bremsung rasch bewegter Teilchen beim Durchgang durch Materie. *Ann. Phys.* **1933**, *16*, 285–320. [[CrossRef](#)]
22. Fano, U. Ionization Yield of Radiations. II. The Fluctuations of the Number of Ions. *Phys. Rev.* **1947**, *72*, 26–29. [[CrossRef](#)]
23. Bohr, N. Scattering and Stopping of Fission Fragments. *Phys. Rev.* **1940**, *58*, 654–655. [[CrossRef](#)]
24. Northcliffe, L.C. Energy Loss and Effective Charge of Heavy Ions in Aluminum. *Phys. Rev.* **1960**, *120*, 1744. [[CrossRef](#)]
25. Firsov, O.B. Interaction Energy of Atoms for Small Nuclear Separations. *J. Exp. Theor. Phys.* **1957**, *5*, 1192–1196.
26. Lindhard, J.; Scharff, M. Energy Dissipation by Ions in the kev Region. *Phys. Rev.* **1961**, *124*, 128–130. [[CrossRef](#)]
27. Fermi, E.; Teller, E. The Capture of Negative Mesotrons in Matter. *Phys. Rev.* **1947**, *72*, 399–408. [[CrossRef](#)]
28. Seitz, F.; Koehler, J.S. *Displacement of Atoms during Irradiation*; Solid State Physics, Seitz, F., Turnbull, D., Eds.; Academic Press: New York, NY, USA, 1956; Volume 2, pp. 305–448.
29. Fleischer, R.; Price, P.; Walker, R. Ion Explosion Spike Mechanism for Formation of Charged-Particle Tracks in Solids. *J. Appl. Phys.* **1965**, *36*, 3645–3652. [[CrossRef](#)]
30. Lifshitz, I.M.; Kaganov, M.I.; Tanatarov, L.V. On the theory of radiation-induced changes in metals. *J. Nucl. Energy A* **1960**, *12*, 69–78. [[CrossRef](#)]
31. Echenique, P.M.; Nieminen, R.M.; Ritchie, R.H. Density functional calculation of stopping power of an electron gas for slow ions. *Solid State Commun.* **1981**, *37*, 779–781. [[CrossRef](#)]
32. Nagy, I.; Arnau, A.; Echenique, P.M.; Zaremba, E. Low-velocity antiproton stopping power. *Phys. Rev. B* **1989**, *40*, 11983–11985. [[CrossRef](#)]
33. Pitarke, J.M.; Ritchie, R.H.; Echenique, P.M. Quadratic response theory of the energy loss of charged particles in an electron gas. *Phys. Rev. B* **1995**, *52*, 13883–13902. [[CrossRef](#)]
34. Nagy, I.; Apagyi, B. Scattering-theory formulation of stopping powers of a solid target for protons and antiprotons with velocity-dependent screening. *Phys. Rev. A* **1998**, *58*, 1653–1656. [[CrossRef](#)]
35. Schleife, A.; Draeger, E.W.; Anisimov, V.M.; Correa, A.A.; Kanai, Y. Quantum Dynamics Simulation of Electrons in Materials on High-Performance Computers. *Comput. Sci. Eng.* **2014**, *16*, 54–61. [[CrossRef](#)]
36. Quijada, M.; Borisov, A.G. Time-dependent density-functional calculation of the stopping power for protons and antiprotons in metals. *Phys. Rev. A* **2007**, *75*, 042902. [[CrossRef](#)]
37. Zeb, M.A.; Kohanoff, J. Electronic Stopping Power in Gold: The Role of d Electrons and the H/He Anomaly. *Phys. Rev. Lett.* **2012**, *108*, 225504. [[CrossRef](#)] [[PubMed](#)]
38. Schleife, A.; Kanai, Y.; Correa, A.A. Accurate atomistic first-principles calculations of electronic stopping. *Phys. Rev. B* **2015**, *91*, 014306. [[CrossRef](#)]
39. Yost, D.C.; Kanai, Y. Electronic stopping for protons and α particles from first-principles electron dynamics: The case of silicon carbide. *Phys. Rev. B* **2016**, *94*, 115107. [[CrossRef](#)]
40. Ullah, R.; Corsetti, F.; Sánchez-Portal, D.; Artacho, E. Electronic stopping power in a narrow band gap semiconductor from first principles. *Phys. Rev. B* **2015**, *91*, 125203. [[CrossRef](#)]
41. Covington, C.; Hartig, K. Time-dependent density-functional-theory investigation of the collisions of protons and α particles with uracil and adenine. *Phys. Rev. A* **2017**, *95*, 052701. [[CrossRef](#)]
42. Yost, D.C.; Kanai, Y. Electronic Excitation Dynamics in DNA under Proton and α -Particle Irradiation. *J. Am. Chem. Soc.* **2019**, *141*, 5241. [[CrossRef](#)]
43. Rubenstein, E.; Bonner, W.A.; Noyes, H.P.; Brown, G.S. Supernovae and Life. *Nature* **1983**, *306*, 118. [[CrossRef](#)]
44. Greenberg, J.M.; Kouchi, A.; Niessen, W.; Irth, H.; Van Paradijs, J.; de Groot, M.; Hermsen, W. Interstellar Dust, Chirality, Comets and the Origins of Life: Life from Dead Stars? *J. Biol. Phys.* **1994**, *20*, 61–70. [[CrossRef](#)]
45. Bailey, J.; Chrysostomou, A.; Hough, J.H.; Gledhill, T.M.; McCall, A.; Clark, S.; Ménard, F.; Tamura, M. Circular Polarization in Star Forming Regions: Implications for Biomolecular Homochirality. *Science* **1998**, *281*, 672–674. [[CrossRef](#)]

46. Meierhenrich, U.J.; Nahon, L.; Alcaraz, C.; Bredehöft, J.H.; Hoffmann, S.V.; Barbier, B.; Brack, A. Asymmetric Vacuum UV photolysis of the Amino Acid Leucine in the Solid State. *Angew. Chem. Int. Ed.* **2005**, *44*, 5630–5634. [[CrossRef](#)] [[PubMed](#)]
47. Munoz Caro, G.M.; Meierhenrich, U.J.; Schutte, W.A.; Barbier, B.; Arcones Segovia, A.; Rosenbauer, H.; Thiemann, W.H.-P.; Brack, A.; Greenberg, J.M. Amino acids from ultraviolet irradiation of interstellar ice analogues. *Nature* **2002**, *416*, 403–406. [[CrossRef](#)] [[PubMed](#)]
48. Takahashi, J.; Kobayashi, K. Origin of Terrestrial Bioorganic Homochirality and Symmetry Breaking in the Universe. *Symmetry* **2019**, *11*, 919. [[CrossRef](#)]
49. Cronin, J.R.; Pizzarello, S. Enantiomeric Excesses in Meteoritic Amino Acids. *Science* **1997**, *275*, 951–955. [[CrossRef](#)]
50. Coolidge, W.D. High Voltage Cathode Rays outside the Generating Tube. *Science* **1925**, *62*, 441–442. [[CrossRef](#)]
51. Lind, S.C.; Bardwell, D.C. The Chemical Action of Gaseous Ions Produced by Alpha Particles VII. *Unsaturated Carbon Compounds. J. Am. Chem. Soc.* **1926**, *48*, 1556–1575. [[CrossRef](#)]
52. Chapiro, A. *Radiation Chemistry of Polymeric Systems*; John Wiley & Sons: New York, NY, USA, 1962.
53. Healy, K.; Schiedt, B.; Morrison, A.P. Solid-state nanopore technologies for nanopore-based DNA analysis. *Nanomedicine* **2007**, *2*, 875–897. [[CrossRef](#)]
54. Sun, J.; Zhang, Y.; Zhong, X.; Zhu, X. Modification of Poly (tetrafluoroethylene) by Radiation-1. Improvement in High Temperature Properties and Radiation Stability. *Radiat. Phys. Chem.* **1994**, *44*, 655–659. [[CrossRef](#)]
55. Toimil-Molares, M.E. Characterization and properties of micro- and nanowires of controlled size, composition, and geometry fabricated by electrodeposition and ion-track technology. *Beilstein J. Nanotechnol.* **2012**, *3*, 860–883. [[CrossRef](#)]
56. Spohr, R. *Ion Tracks and Microtechnology Principles and Applications*; Bethge, K., Ed.; Vieweg GmbH: Kranzberg, Germany, 1990.
57. Tylka, A.J.; Adams, J.H.; Boberg, P.R.; Brownstein, B.; Dietrich, W.F.; Flueckiger, E.O.; Petersen, E.L.; Shea, M.A.; Smart, D.F.; Smith, E.C. CREME96: A Revision of the Cosmic Ray Effects on Micro-Electronics Code. *IEEE Trans. Nucl. Sci.* **1997**, *44*, 2150–2160. [[CrossRef](#)]
58. Suzuki, Y.; Maekawa, Y.; Yoshida, M.; Maeyama, K.; Yonezawa, N. Ion-Beam-Induced Dual-Tone Imaging of Polyimide via Two-Step Imidization. *Chem. Mater.* **2002**, *14*, 4186–4191. [[CrossRef](#)]
59. Rauber, M.; Alber, I.; Muller, S.; Neumann, R.; Picht, O.; Roth, C.; Schokel, A.; Toimil-Molares, M.E.; Ensinger, W. Highly-Ordered Supportless Three-Dimensional Nanowire Networks with Tunable Complexity and Interwire Connectivity for Device Integration. *Nano Lett.* **2011**, *11*, 2304–2310. [[CrossRef](#)] [[PubMed](#)]
60. Wang, P.; Wang, M.; Liu, F.; Ding, S.; Wang, X.; Du, G.; Liu, J.; Apel, P.; Kluth, P.; Trautmann, C.; et al. Ultrafast ion sieving using nanoporous polymeric membranes. *Nat. Commun.* **2018**, *9*, 569. [[CrossRef](#)] [[PubMed](#)]
61. Yoshida, M.; Kimura, Y.; Chen, J.; Asano, M.; Maekawa, Y. Preparation of PTFE-based fuel cell membranes by combining latent track formation technology with graft polymerization. *Radiat. Phys. Chem.* **2009**, *78*, 1060–1066. [[CrossRef](#)]
62. Pérez-Mitta, G.; Marmisollé, W.A.; Trautmann, C.; Toimil-Molares, M.E.; Azzaroni, O. Nanofluidic Diodes with Dynamic Rectification Properties Stemming from Reversible Electrochemical Conversions in Conducting Polymers. *J. Am. Chem. Soc.* **2015**, *137*, 15382–15385. [[CrossRef](#)]
63. Pérez-Mitta, G.; Albesa, A.G.; Knoll, W.; Trautmann, C.; Toimil-Molares, M.E.; Azzaroni, O. Host-guest supramolecular chemistry in solid-state nanopores: Potassium-driven modulation of ionic transport in nanofluidic diodes. *Nanoscale* **2015**, *7*, 15594–15598. [[CrossRef](#)]
64. Spende, A.; Sobel, N.; Lukas, M.; Zierold, R.; Riedl, J.C.; Gura, L.; Schubert, I.; Montero Moreno, J.M.; Nielsch, K.; Stühn, B.; et al. TiO₂, SiO₂, and Al₂O₃ coated nanopores and nanotubes produced by ALD in etched ion-track membranes for transport measurements. *Nanotechnology* **2015**, *26*, 335301. [[CrossRef](#)]
65. Yameen, B.; Ali, M.; Neumann, R.; Ensinger, W.; Knoll, W.; Azzaroni, O. Ionic transport through single solid-state nanopores controlled with thermally nanoactuated macromolecular gates. *Small* **2009**, *5*, 1287–1291. [[CrossRef](#)]
66. Amemiya, K.; Koshikawa, H.; Yamaki, T.; Maekawa, Y.; Shitomi, H.; Numata, T.; Kinoshita, K.; Tanabe, M.; Fukuda, D. Fabrication of hard-coated optical absorbers with microstructured surfaces using etched ion tracks: Toward broadband ultra-low reflectance. *Nucl. Instr. Methods Phys. Res. B* **2015**, *356–357*, 154–159. [[CrossRef](#)]
67. Dole, B. *The Radiation Chemistry of Macromolecules*; Academic Press: New York, NY, USA, 1972; Volume 1.

68. Bledzki, A.K.; Gassan, J. Composites reinforced with cellulose based fibres. *Polym. Sci.* **1999**, *24*, 221–274. [[CrossRef](#)]
69. Flory, P.J. Thermodynamics of High Polymer Solutions. *J. Chem. Phys.* **1942**, *10*, 51–61. [[CrossRef](#)]
70. Pfeuty, P.; Velasco, R.M.; de Gennes, P.G. Conformation properties of one isolated polyelectrolyte chain in D dimensions. *J. Phys. Lett.* **1977**, *38*, 5–7. [[CrossRef](#)]
71. De Gennes, P.G.; Léger, L. Dynamics of Entangled Polymer Chains. *Ann. Rev. Phys. Chem.* **1982**, *33*, 49–61. [[CrossRef](#)]
72. Charlesby, A. The Crosslinking and Degradation of Paraffin Chains by High-Energy Radiation. *Proc. R. Soc. Lond. A* **1954**, *222*, 60–74.
73. Hatano, Y.; Katsumura, Y.; Mozumder, A. *Charged Particle and Photon. Interactions with Matter: Recent Advances, Applications, and Interfaces*; CRC Press: Boca Raton, FL, USA, 2010.
74. Magee, J.L.; Chatterjee, A. Radiation Chemistry of Heavy-Particle Tracks. 1. General Considerations. *J. Phys. Chem.* **1980**, *84*, 3529–3536. [[CrossRef](#)]
75. Freeman, G.R. *Kinetics of Nonhomogeneous Processes*; John Wiley & Sons: Toronto, ON, Canada, 1987.
76. Fleischer, R.L.; Price, P.B.; Walker, R.M. Tracks of Charged Particles in Solids. *Science* **1965**, *149*, 383–393. [[CrossRef](#)]
77. Chatterjee, A.; Schaefer, H.J. Microdosimetric Structure of Heavy Ion Tracks in Tissue. *Radiat. Environ. Biophys.* **1976**, *13*, 215–227. [[CrossRef](#)]
78. Seki, S.; Tsukuda, S.; Maeda, K.; Tagawa, S.; Shibata, H.; Sugimoto, M.; Jimbo, K.; Hashitomi, I.; Koyama, A. Effects of Backbone Configuration of Polysilanes on Nanoscale Structures Formed by Single-Particle Nanofabrication Technique. *Macromolecules* **2005**, *38*, 10164–10170. [[CrossRef](#)]
79. Seki, S.; Tagawa, S. Optoelectronic Properties and Nanostructure Formation of σ -Conjugated Polymers. *Polym. J.* **2007**, *39*, 277–293. [[CrossRef](#)]
80. Flory, P.J. The Configuration of Real Polymer Chains. *J. Chem. Phys.* **1949**, *17*, 303–310. [[CrossRef](#)]
81. Tsukuda, S.; Seki, S.; Tagawa, S. Effect of ion beam energy and polymer weight on the thickness of nanowires produced by ion bombardment of polystyrene thin films. *Appl. Phys. Lett.* **2005**, *87*, 233119. [[CrossRef](#)]
82. Tsukuda, S.; Seki, S.; Tagawa, S.; Sugimoto, M. Correlation between Edge Roughness of Nanostructures and Backbone Configuration of Polymer Materials. *J. Photopolym. Sci. Technol.* **2005**, *18*, 449–450.
83. Seki, S.; Tsukuda, S.; Tagawa, S.; Sugimoto, M. Correlation between Roughness of Nanowires and Polymer Backbone Conformation. *Macromolecules* **2006**, *39*, 7446–7450. [[CrossRef](#)]
84. Horio, A.; Sakurai, T.; Kayama, K.; Lakshmi, G.B.V.S.; Avasthi, D.K.; Sugimoto, M.; Yamaki, T.; Chiba, A.; Saito, Y.; Seki, S. Remarkable Effect of Halogenation of Aromatic Compounds on Efficiency of Nanowire Formation through Polymerization/Crosslinking by High-Energy Single Particle Irradiation. *Radiat. Phys. Chem.* **2018**, *142*, 100–106. [[CrossRef](#)]
85. Modelli, A.; Jones, D. Empty level structure and dissociative electron attachment cross sections in bromo and chloro dihaloalkanes. *J. Phys. Chem. A* **2009**, *113*, 7795–7801. [[CrossRef](#)]
86. Kim, N.; Sohn, T.; Lee, S.H.; Nandi, D.; Kim, S.K. Atomic selectivity in dissociative electron attachment to dihalobenzenes. *Phys. Chem. Chem. Phys.* **2013**, *15*, 16503–16509. [[CrossRef](#)]
87. Tsukuda, S.; Seki, S.; Sugimoto, M.; Tagawa, S. Formation of Nanowires Based on π -Conjugated Polymers by High-Energy Ion Beam Irradiation. *Jpn. J. Appl. Phys.* **2005**, *44*, 5839–5842. [[CrossRef](#)]
88. Tsukuda, S.; Seki, S.; Sugimoto, M.; Tagawa, S.; Tanaka, S.-I. SiC nanowires formed by high energy ion beam irradiation to polymer films and heating. *J. Ceram. Proc. Res.* **2008**, *9*, 466–469.
89. Tsukuda, S.; Seki, S.; Sugimoto, M.; Tagawa, S. Customized Morphologies of Self-Condensed Multisegment Polymer Nanowires. *J. Phys. Chem.* **2006**, *110*, 19319–19322. [[CrossRef](#)]
90. Omichi, M.; Marui, H.; Takano, K.; Tsukuda, S.; Sugimoto, M.; Kuwabata, S.; Seki, S. Temperature-Responsive One-Dimensional Nanogels Formed by the Cross-Linker-Aided Single Particle Nanofabrication Technique. *ACS Appl. Mater. Interfaces* **2012**, *4*, 5492–5497. [[CrossRef](#)]
91. Omichi, M.; Marui, H.; Padalkar, V.S.; Horio, A.; Tsukuda, S.; Sugimoto, M.; Seki, S. Fabrication of Thermoresponsive Nanoactinia Tentacles by a Single Particle Nanofabrication Technique. *Langmuir* **2015**, *31*, 11692–11700. [[CrossRef](#)] [[PubMed](#)]
92. Cheng, H.L.; Tang, M.T.; Tuchinda, W.; Enomoto, K.; Chiba, A.; Saito, Y.; Kamiya, T.; Sugimoto, M.; Saeki, A.; Sakurai, T.; et al. Reversible Control of Radius and Morphology of Fluorene-Azobenzene Copolymer Nanowires by Light Exposure. *Adv. Mater. Interfaces* **2014**, *2*, 1400450. [[CrossRef](#)]

93. Tsukuda, S.; Seki, S.; Saeki, A.; Kozawa, T.; Tagawa, S.; Sugimoto, M.; Idesaki, A.; Tanaka, S. Precise Control of Nanowire Formation Based on Polysilane for Photoelectronic Device Application. *Jpn. J. Appl. Phys.* **2004**, *43*, 3810–3814. [[CrossRef](#)]
94. Seki, S.; Saeki, A.; Choi, W.; Maeyoshi, Y.; Omichi, M.; Asano, A.; Enomoto, K.; Vijayakumar, C.; Sugimoto, M.; Tsukuda, S.; et al. Semiconducting Cross-Linked Polymer Nanowires Prepared by High-Energy Single-Particle Track Reactions. *J. Phys. Chem. B* **2012**, *116*, 12857–12863. [[CrossRef](#)]
95. Wasin, T.; Enomoto, K.; Sakurai, T.; Padalkar, V.S.; Cheng, H.L.; Tang, M.T.; Horio, A.; Sakamaki, D.; Omichi, M.; Saeki, A.; et al. Fabrication of “Clickable” Polyfluorene Nanowires with High Aspect Ratio as Biological Sensing Platforms. *ACS Sens.* **2016**, *1*, 766–774. [[CrossRef](#)]
96. Omichi, M.; Asano, A.; Tsukuda, S.; Takano, K.; Sugimoto, M.; Saeki, A.; Sakamaki, D.; Onoda, A.; Hayashi, T.; Seki, S. Fabrication of enzyme-degradable and size-controlled protein nanowires using single particle nano-fabrication technique. *Nat. Commun.* **2014**, *5*, 3718. [[CrossRef](#)]
97. Asano, A.; Omichi, M.; Tsukuda, S.; Takano, K.; Sugimoto, M.; Saeki, A.; Seki, S. Fabrication and Arrangement of “Clickable” Nanowires by the Single-Particle Nanofabrication Technique. *J. Phys. Chem. C* **2012**, *116*, 17274–17279. [[CrossRef](#)]
98. Asano, A.; Maeyoshi, Y.; Watanabe, S.; Saeki, A.; Sugimoto, M.; Yoshikawa, M.; Nanto, H.; Tsukuda, S.; Tanaka, S.; Seki, S. Sugar nanowires based on cyclodextrin on quartz crystal microbalance for gas sensing with ultra-high sensitivity. *Radiat. Phys. Chem.* **2013**, *84*, 196–199. [[CrossRef](#)]
99. Omichi, M.; Choi, W.; Sakamaki, D.; Tsukuda, S.; Sugimoto, M.; Seki, S. A simple and rapid method for high-resolution visualization of single-ion tracks. *AIP Adv.* **2014**, *4*, 117128. [[CrossRef](#)]
100. Seki, S.; Tsukuda, S.; Tagawa, S.; Sugimoto, M.; Watanabe, A.; Miyashita, T. Formation of Isolated Ultrafine Optical Nanofibers by Single Particle Nanofabrication Technique. *J. Photopolym. Sci. Tech.* **2007**, *20*, 125–128. [[CrossRef](#)]
101. Takeshita, Y.; Sakurai, T.; Asano, A.; Takano, K.; Omichi, M.; Sugimoto, M.; Seki, S. Formation of nanowires from pentacene derivatives by single-particle triggered linear polymerization. *Adv. Mater. Lett.* **2015**, *6*, 99–103. [[CrossRef](#)]
102. Onoe, J.; Nakao, A.; Takeuchi, K. XPS study of a photopolymerized C₆₀ film. *Phys. Rev. B* **1997**, *55*, 10051–10056. [[CrossRef](#)]
103. Onoe, J.; Nakayama, T.; Aono, M.; Hara, T. Structural and electrical properties of an electron-beam-irradiated film. *Appl. Phys. Lett.* **2003**, *82*, 595–597. [[CrossRef](#)]
104. Onoe, J.; Nakayama, T.; Aono, M.; Hara, T. Electrical properties of a two-dimensionally hexagonal photopolymer. *J. Appl. Phys.* **2004**, *96*, 443. [[CrossRef](#)]
105. Bajwa, N.; Ingale, A.; Avasthi, D.K.; Kumar, R.; Tripathi, A.; Dharamvir, K.; Jindal, V.K. Role of electron energy loss in modification of C₆₀ thin films by swift heavy ions. *J. Appl. Phys.* **2008**, *104*, 054306. [[CrossRef](#)]
106. Kumar, A.; Avasthi, D.K.; Tripathi, A.; Kabiraj, D.; Singh, F.; Pivin, J.C. Synthesis of confined electrically conducting carbon nanowires by heavy ion irradiation of fullerene thin film. *J. Appl. Phys.* **2007**, *101*, 014308. [[CrossRef](#)]
107. Kumar, A.; Avasthi, D.K.; Tripathi, A.; Filip, L.D.; Carey, J.D.; Pivin, J.C. Formation and characterization of carbon nanowires. *J. Appl. Phys.* **2007**, *102*, 044305. [[CrossRef](#)]
108. Kumar, A.; Singh, F.; Tripathi, A.; Pernot, J.; Pivin, J.C.; Avasthi, D.K. Conducting carbon nanopatterns (nanowire) by energetic ion irradiation. *J. Phys. D Appl. Phys.* **2008**, *41*, 095304. [[CrossRef](#)]
109. Maeyoshi, Y.; Saeki, A.; Suwa, S.; Omichi, M.; Marui, H.; Asano, A.; Tsukuda, S.; Sugimoto, M.; Kishimura, A.; Kataoka, K.; et al. Fullerene nanowires as a versatile platform for organic electronics. *Sci. Rep.* **2012**, *2*, 600. [[CrossRef](#)]
110. Mittal, V.K.; Lotha, S.; Avasthi, D.K. Hydrogen loss under heavy ion irradiation in polymers. *Radiat. Eff. Defects Solids* **1999**, *147*, 199–209. [[CrossRef](#)]
111. Sreenath, K.; Suneesh, C.V.; Kumar, V.K.R.; Gopidas, K.R. Cu (II)-Mediated Generation of Triarylamine Radical Cations and Their Dimerization. An Easy Route to Tetraarylbenzidines. *J. Org. Chem.* **2008**, *73*, 3245–3251. [[CrossRef](#)] [[PubMed](#)]
112. Horio, A.; Sakurai, T.; Lakshmi, G.B.V.S.; Avasthi, D.K.; Sugimoto, M.; Yamaki, T.; Seki, S. Formation of nanowires via single particle-triggered linear polymerization of solid-state aromatic molecules. *Nanoscale* **2016**, *8*, 14925–14931. [[CrossRef](#)]

113. Li, L.; Liu, X.; Pal, S.; Wang, S.; Ober, C.K.; Giannelis, E.P. Extreme ultraviolet resist materials for sub-7 nm patterning. *Chem. Soc. Rev.* **2017**, *46*, 4855–4866. [[CrossRef](#)] [[PubMed](#)]
114. Sakaguchi, S.; Sakurai, T.; Ma, J.; Sugimoto, M.; Yamaki, T.; Chiba, A.; Saito, Y.; Seki, S. Conjugated Nanowire Sensors via High-Energy Single-Particle-Induced Linear Polymerization of 9,9'-Spirobi[9 *H*-fluorene] Derivatives. *J. Phys. Chem. B* **2018**, *122*, 8614–8623. [[CrossRef](#)] [[PubMed](#)]



© 2020 by the authors. Licensee MDPI, Basel, Switzerland. This article is an open access article distributed under the terms and conditions of the Creative Commons Attribution (CC BY) license (<http://creativecommons.org/licenses/by/4.0/>).